J. Fluid Mech. (1971), *vol.* 48, *part* 1, *pp.* 91–127
Printed in Great Britain

Measurements of atmospheric pressure on wind-generated sea waves

By FRED W. DOBSON†

Institute of Oceanography, University of British Columbia, Vancouver, Canada

(Received 26 September 1970)

Simultaneous measurements of wave elevation and atmospheric pressure on wind-driven sea waves were made using a vertical wave-sensing rod and a small (23 cm diameter) pancake-shaped styrofoam buoy in which was embedded a sensitive pressure transducer; the wave probe constrained the buoy to move with the waves only in the vertical direction. Care was taken to avoid contamination of the pressure signal with dynamic pressures caused by flow distortion around the buoy.

Results are presented as power and cross-spectra of wave elevation and pressure, spectra of the fluxes of energy and momentum from the wind to the waves, and spectra of ζ, the fractional increase in wave energy per radian.

The phase shifts of the pressure signal are compared with the laboratory and field results of other investigators, and with the theoretical predictions of Miles's (1957) inviscid laminar model of wave growth. Agreement is reasonably good among the experimental results, but observed phase shifts are an order of magnitude larger than the theoretically predicted values.

Integrals under the momentum flux spectra are compared in all runs with the predictions of the standard empirical formula, and in two cases are compared with the values of the total wind stress as measured with a sonic anemometer; the indication is that a large fraction of the total flux of momentum from the air to the sea goes initially into the wave field.

The ζ spectra are compared with the field results of Snyder & Cox (1966) and with the theoretical predictions of Miles's (1957) model; agreement is again good between the field results while the theory underpredicts ζ by factors of between 5 and 8.

A simple dimensionless relation is found between ζ and the ratio of wind speed to wave phase speed.

1. Introduction

With the purpose of obtaining simultaneous measurements of fluctuations of pressure and of wave height on wind-driven waves, a small buoy containing a pressure sensor was allowed to float on the water surface, being constrained by a vertical wave-sensing rod to move only vertically. The pressure and wave height

† Present address: Atlantic Oceanographic Laboratory, Bedford Institute, Dartmouth, Nova Scotia, Canada

signals so obtained were analyzed to give their power and cross-spectra, giving, among other quantities, the phase relationship of the pressure and wave signals and the energy and momentum fluxes from the wind to the waves.

The reasons for attempting such an obviously formidable measurement were compelling. It has long been surmised (Stewart 1961) that most of the energy transfer from the wind to the waves occurs through the action of normal pressures in quadrature with the wave height. By making reliable measurements in the field the correspondence with reality of extant theories could be judged and a data base laid for future theoretical work. As pointed out by Stewart (1967), the most important manifestations of wave generation in the air flow above the waves appear to occur at very small heights above the instantaneous water surface; therefore any measurements taken close to the surface are of considerable value. The cross-spectra between pressure and wave height contain the information necessary for computing the fluxes of energy and momentum to the waves; thus if measurements were also made of the *total* momentum flux to the sea surface, it would become possible to compare the size of the two fluxes; this comparison had never been made directly.

Only two other attempts have been made to measure normal pressures on sea waves, Longuet-Higgins, Cartwright & Smith (1963) and Kolesnikov & Efimov (1962). The results obtained from both these attempts may be in error, since on both buoys the pressure-sensing orifice was so placed that it must have been subjected to fluctuations in dynamic pressure caused by the tilting of the buoy relative to the water surface (it is easy to show, using potential flow theory and regarding the buoy as a segment of a sphere projecting above the water surface, that small buoy tilts cause pressure variations at an orifice at the top of the buoy which are a sizable fraction of the stagnation pressure $\frac{1}{2}\rho U^2$, where ρ is air density and U is the wind speed near the water surface).

In the present experiment considerable effort was put into developing an effective scheme for rejecting dynamic pressures. The final model of the buoy used in the experiments was tested carefully in a wind tunnel and against other sensors at a land site (Dobson 1969). In addition, the buoy was not free-floating, being constrained to move only vertically, thus eliminating the necessity of assuming that errors introduced by treating Lagrangian data as if they were Eulerian are small.

2. Theory

This experiment was designed to measure wave-induced pressure fluctuations at the sea surface. There are two published theories, those of Jeffreys (1925) and Miles (1957, 1959), which propose physically realistic mechanisms for wave growth and which predict wave-induced pressures; the predictions of the two models will be outlined for reference purposes.

2.1. *Jeffreys and flow separation*

Jeffreys (1925) assumed that as air flows over sea waves separation occurs on the leeward sides of the wave crests, with re-attachment occurring somewhere down

the leeward slopes. This produces low ambient pressures on the downwind slopes, and hence a net transfer of energy and momentum to the waves.

Jeffreys took p^*, the component of pressure in quadrature with η, the wave elevation, to be

$$p^* = s\rho_a(U-c)^2\,\partial\eta/\partial x$$
$$= -s\rho_a\frac{(U-c)^2}{c}\,\partial\eta/\partial t, \tag{2.1}$$

where ρ_a is air density, U is the mean wind speed, c is the wave phase velocity, and where $\partial/\partial t = -c\,\partial/\partial x$ has been used. The size of Jeffreys's 'sheltering coefficient' s is still a subject of controversy; in fact, the whole question of whether or not separation actually occurs over sea waves is still being argued (Wu 1970). One argument against the existence of separation has been put forward by Lighthill (1962), who observed that since waves have a finite phase speed, therefore close to the water surface the air is moving more slowly than the wave crests and that separation, if it did exist, might be expected to occur to windward of the wave crests. Since, however, this argument relies on a fairly large ratio c/U of wave phase speed to wind speed, it might be expected to break down at high wind speeds and for slow, short-wavelength waves. Both Plate, Chang & Hidy (1969) and Wu (1970) observe phenomena apparently associated with flow separation in their wind-wave tunnels at low values of c/U.

For large c/U the only form of 'separation' which can be said to occur is of the type suggested by Lighthill, and it must occur then not at the water surface, but at the 'critical' height z_c where $U = c$.

2.2. *Miles and shear flow instability*

The idea that momentum and energy might be transferred from the wind to sea waves by means of instability of the mean shear flow in the air was first advanced by Miles in 1957; he reformulated his theory once in 1959 to include viscous effects and again in 1960 to include, as a wave initiation mechanism, a model proposed by Phillips (1957), whereby waves were started and made to grow through the action of incoherent turbulent pressure fluctuations. Benjamin (1959) and Lighthill (1962) have added considerably to the physical and mathematical completeness of Miles's theory.

More recently, the theory has been reviewed by Phillips (1966), Miles (1967), Stewart (1967) and Davis (1969, 1970). The reviews dealt with two basic objections. First, a growing body of experimental evidence indicates that the model underpredicts wave growth by one order of magnitude. Secondly, the model assumed that interactions of the turbulent and wave-induced Reynolds stresses could be neglected.

It may be that the first objection is a direct result of the second, and the recent work of Stewart (1970) and Davis (1970) has been aimed at determining the vertical structure of the wind field and of the turbulent and wavy Reynolds stresses, and the variation of the above quantities with wave phase, with the hope of obtaining a better understanding of the effects of turbulence and viscosity on the flow structure close to the waves.

It is hoped that the present measurements, which are the first accurate field measurements of one of the aerodynamic parameters made actually on the surface of the waves, will provide a useful data base against which the predictions of new theories or reformulations of old ones may be judged.

The basic shear flow instability mechanism, called by Miles his 'inviscid laminar' model, was formulated in terms of a sinusoidal wave train moving with phase speed c underneath a mean vertical wind profile which varied logarithmically with height. Viscous and turbulence effects were neglected, except for viscous stresses in the vicinity of the surface and the critical layer, and for the assumption of the presence of turbulence implicit in the use of a logarithmic profile.

Miles proposed a wave-induced pressure

$$p' = (\alpha + i\beta)\rho_a U_1^2 k\eta, \tag{2.2}$$

where

$$\eta = a e^{ik(x-ct)}, \tag{2.3}$$

ρ_a is the air density and U_1 is a 'reference velocity' defined for the case of a logarithmic wind profile by

$$\begin{aligned} U(z) &= U_1 \ln (z/z_0) \\ &= \frac{u_*}{K} \ln (z/z_0), \end{aligned} \tag{2.4}$$

where

$$u_* = (\tau/\rho_a)^{\frac{1}{2}} \tag{2.5}$$

is the friction velocity of the air flow, τ is the momentum flux from air to water, $K\,(\simeq 0{\cdot}4)$ is von Karman's constant, and z_0 is a 'roughness length' (see, for instance, Lumley & Panofsky 1964).

It is the term

$$\begin{aligned} p^* &= i\beta\rho_a U_1^2 k\eta \\ &= -\beta\rho_a \frac{U_1^2}{c} \partial\eta/\partial t \end{aligned} \tag{2.6}$$

which causes the waves to grow exponentially with time according to

$$a^2(t) = a_0^2 e^{\omega\zeta t}, \tag{2.7}$$

where $\omega = 2\pi f$ is radian frequency and

$$\zeta = \frac{\partial E}{\partial t} \Big/ \omega E \tag{2.8}$$

$$= \rho_a/\rho_w (U_1/c)^2 \beta \tag{2.9}$$

is the fractional increase in wave energy E per radian.

Miles's solution for the wave-induced Reynolds stress is

$$\begin{aligned} -\rho_a \overline{\mathscr{U}\mathscr{W}} &= -\rho_a [(\pi U_{zz}/kU_z)\,\overline{\mathscr{W}^2}]_{z_c} \quad (z < z_c), \\ &= 0 \quad (z > z_c); \end{aligned} \tag{2.10}$$

from this and (2.8)

$$\zeta = -\frac{\rho_a}{\rho_w} [(\pi U_{zz}/kU_z)\,\overline{\mathscr{W}^2}]_{z_c} \div \overline{(\partial\eta/\partial t)^2}, \tag{2.11}$$

where the z subscripts denote differentiation with respect to z and the quantities in the square brackets are evaluated at the critical height z_c.

Miles (1959) carried out a numerical integration of the inviscid form of the Orr–Sommerfeld equation using a logarithmic wind speed profile to obtain β and hence ζ, as well as α and hence the predicted phase θ of the wave-induced pressures

$$\theta = \tan^{-1}(\beta/-\alpha). \tag{2.12}$$

Longuet-Higgins *et al.* (1963) have modified (2.12) to account for the pressures $\rho_a g\eta(t)$ associated with the vertical motion of the buoy; the predicted phase then becomes

$$\theta_b = \tan^{-1}\left[\frac{\beta(U_1/c)^2}{1-\alpha(U_1/c)^2}\right]. \tag{2.13}$$

3. The experiment

The individual parts of the measurement system will be outlined first; then the operation of the whole system will be described.

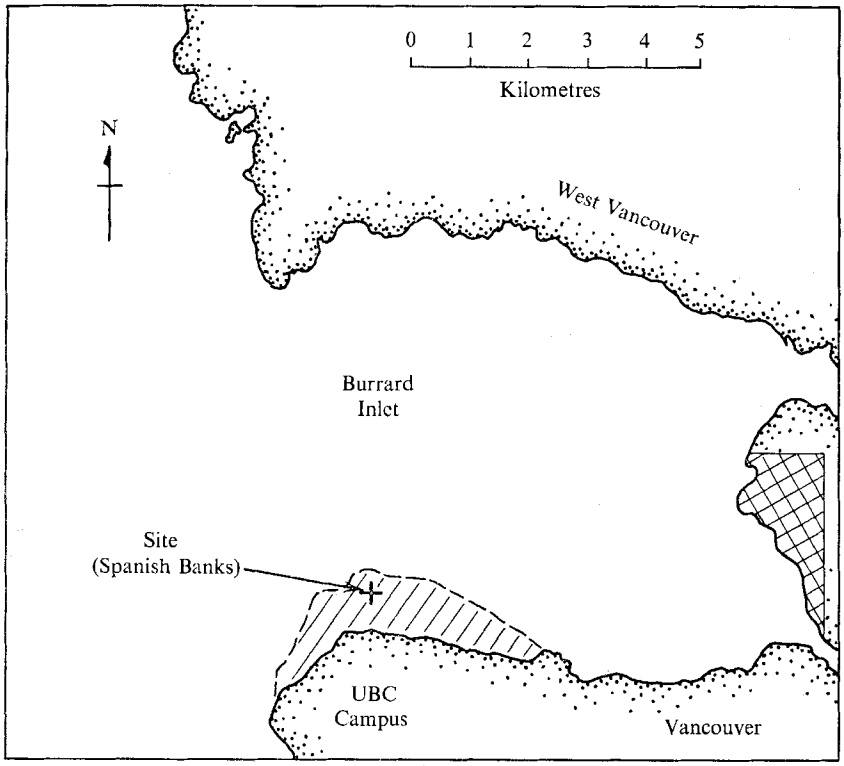

FIGURE 1. Spanish Banks experimental site.

3.1. *Site*

The site (figure 1) consisted of a recording platform, and a mast of 10 cm diameter and 6 m high located about 80 m to the north of the platform. Both were on a tidal sand flat which was covered by 2–3 m of water at high tide. Fetches to the

west were 40–60 km, and to the east were 2–8 km (almost all the runs used were taken in easterly and south-easterly winds). On the point of land to the east of the site is situated a 'forest' of 30–40 large apartment buildings about 80 m in height.

3.2. *The wave probe*

The wave probe used was of the capacitance type, similar to that used by Kinsman (1960); it consisted of a $\frac{1}{4}$ in. stock (0·635 cm O.D.) rod 180 cm in length coated with teflon tubing and attached to an aluminium frame. The rod acted as a cylindrical condenser with a sea water return which modulated the frequency of a blocking oscillator as the water height changed. Its signal (and all other signals of the system) was recorded in analogue form on Ampex 'CP-100' or 'FR-1300' 14-channel instrumentation tape recorders. The estimated uncertainty in the wave measurement system is ± 2 mm.

The wave probe also acted as a guide for the buoy, which slid vertically on it using a teflon bearing to which the buoy was attached with gymbals.

3.3. *The pressure sensor*

The sensor package used to measure pressure had to be designed specifically for the experiment; no existing commercial sensor with the required frequency response, small size, and light weight was available.

The electronics carried by the buoy (figure 2, plate 1) consisted of a small capacitance microphone (the pressure sensor) which modulated the frequency of a 100 MHz clapp oscillator; a buffer amplifier; and a 15 V carbon–zinc battery. The complete package, including the battery to power the electronics, weighed less than 200 g and occupied a volume of less than 100 cm^3. The FM output from the buffer was carried by a thin, flexible length of coaxial cable (RG 174/U) to an instrument mast, where it was amplified and sent to the recording platform 80 m distant for demodulation and storage on magnetic tape.

The frequency response of the pressure sensor was set to produce maximum phase deviations of less than 10 degrees from 0·1 to 1 Hz, so that the phase measurement could be as accurate as possible. The low-frequency cut-off of the sensor was therefore set at about 0·05 Hz with a pneumatic filter consisting of a slow leak around the microphone diaphragm feeding a 'back-up' volume. To avoid aliasing during digitization the upper frequency cut-off of all signals was set at 6 Hz using matched two-stage constant time delay electronic filters.

It proved impractical to try to keep water away from the pressure-sensing orifice on the buoy surface for more than a few seconds at a time; therefore the orifice was sealed with a thin rubber diaphragm. To allow the pressure inside the system to equalize with ambient conditions a leak with a time constant of 50 sec was provided from the back-up volume to atmospheric pressure. This arrangement was less than ideal because the rubber diaphragm cut the pressure sensitivity of the system in half and because unavoidable pressure build-ups in the system caused the diaphragm tension to change, leading to variations in the pressure sensitivity of the instrument. This made field calibrations necessary, and these were taken at least once for each run; the end result was an unavoidable degradation in the accuracy of the pressure amplitude measurements, but not of the

phase measurements (except for the case where the pressure signal was corrected for vertical movements of the buoy in the atmospheric pressure gradient).

The laboratory calibration of the pressure system was accomplished by sinusoidally varying the pressure in a drum containing the buoy and a standard sensor; both the amplitude and frequency of the drum pressure could be varied. The laboratory calibration of the system as used in the field is shown in figure 3 (*a*); note the small scatter in the phase results. The field calibrations consisted of raising and lowering the buoy through a known distance in the atmospheric pressure gradient and recording the resulting pressure signals.

The noise of the sensing and recording system could not be neglected, and in some cases noise peaks appeared in the spectra. This unwelcome situation arose out of the requirement that the frequency response of the system extend to frequencies well below the range of interest; as a result large drifts, presumably caused by temperature changes in the back-up volume, were common and little or no amplification of the signal was possible before recording. The wide band noise of the system, including the electronics, recording, rerecording, and digitization but excluding the microphone itself, was equivalent to a pressure signal of less than 2 μbar (1 μbar equals 1 dyne cm^{-2}) peak-to-peak.

3.4. *The buoy*

The diameter of the buoy (figure 2, plate 1) is 23 cm, and the pressure port, seen as a dark circular area near the central hole in the buoy, is 2·4 cm above the water surface (the scale on its surface is 15 cm long). The buoy is hinged so it can respond to short, steep waves. The tail fin keeps the bow pointing into the wind. The thin half-ring to leeward of the pressure port is the device used to cancel the dynamic suction pressure associated with the air flow over the bow of the buoy. The buoy is attached to the wave probe, which is the vertical rod shown at the buoy centre. The electronics and the microphone are beneath a perspex slab extending from the bow to the ring.

The buoy used was the final model of several prototypes, all of which were tested for sea-keeping ability at the site on wind-generated waves. Slow-motion moving pictures were used extensively during these tests to optimize the response of the buoy to the moving water surface. The final prototype was found to take up attack angles (angles of tilt relative to the instantaneous water surface) less than ± 5 degrees for more than 90 % of the time in wind-driven waves at wind speeds of up to 5 m per sec.

3.5. *Aerodynamic calibration of the buoy*

One of the principal difficulties associated with making measurements of any type is to ensure that the sensor itself does not materially interfere with the process it has been designed to observe. This is particularly true in the measurement of pressure; any disturbance of the streamlines of the flow under observation induces dynamic pressures associated with accelerations of the fluid around the disturbing body; their magnitude is some fraction of the stagnation pressure $p_d = \frac{1}{2}\rho_a U^2$, the fraction increasing with the severity of the disturbance.

In the case of the buoy, which in order to stay afloat at all had a rather bluff

bow, the dynamic pressure was about $-0{\cdot}2p_d$ at the pressure port. To cancel this a thin half-ring (3 mm high) was fixed on the buoy surface to leeward of the pressure port. This ring produced a pressure of $+0{\cdot}2p_d$ at the pressure port. Because of its circular symmetry the ring caused effective cancellation of the dynamic pressure over angles of orientation of ± 30 degrees.

The aerodynamic calibration of the buoy was carried out in the low-speed wind tunnel of the UBC Department of Mechanical Engineering. A Datametrics 'Barocel' pressure sensor was used for these tests; its known accuracy was $\pm 0{\cdot}2$ dyne cm^{-2}. The tests consisted of varying the tilt and orientation of the buoy used in the field with respect to the wind-tunnel floor and the wind direction respectively, at different wind speeds, and measuring pressure at various locations on the centre-line of the buoy. To match conditions in the field as closely as possible, the wind-tunnel boundary layer was artificially tripped 1·7 metres upstream of the buoy. This produced a boundary-layer thickness Reynolds number of 5×10^4 and a wind-speed profile which obeyed the law of the wall

$$U/u_* = f(zu_*/v_a), \tag{3.1}$$

where U and u_* are the free-stream air velocity and the friction velocity $(\tau/\rho_a)^{\frac{1}{2}}$ respectively, z is the height, and v_a the kinematic viscosity; the profile exhibited a straight line on a plot of U/u_* versus $\log(zu_*/v_a)$ over the range

$$1 \leqslant \log(zu_*/v_a) \leqslant 3{\cdot}6.$$

The aerodynamic calibration of the buoy resulting from the wind-tunnel tests is shown in figure 3(*b*). The pressure observed at the sensing orifice used in the field is plotted as a fraction of p_d versus wind speed for various tilt angles θ_t. Stalling occurred at low wind speeds for tilt angles greater than $+10$ degrees; no measurements were taken at angles less than -5 degrees since for larger negative angles the bow of the buoy would be submerged.

Care was taken to ensure that the configuration of tilted buoy and wind-tunnel floor were as they would be if the buoy were floating on a water surface. No attempt, however, was made to put the buoy in a curved flow such as exists over waves. The error caused by flow curvature is proportional to the ratio of buoy diameter to the radius of curvature of the flow; this error is discussed in § 4 as the error caused by finite buoy size.

It is clear from figure 3(*b*) that the dynamic pressures were more than 95% rejected for wind speeds up to 6 m sec^{-1} at attack angles from -5 to $+10$ degrees.

To gain an idea of the importance of contamination by dynamic pressures, their size can be compared with Miles's (1959) prediction for the amplitude of the pressures coherent with the waves. Taking a value of $U_1 = 2{\cdot}5u_* \simeq U_5/12$ and a 'reasonable' value of the r.m.s. wave slope $\{(ka)^2\}^{\frac{1}{2}}$ of about 0·1 (see, for instance, Stewart 1967), substitution in (2.2) with a value for $(\alpha^2+\beta^2)^{\frac{1}{2}}$ of about 10 gives, for a 5 m sec^{-1} wind,

$$p' \simeq 2 \text{ dyne cm}^{-2}.$$

In a turbulent wind field the expected dynamic pressure is

$$p_d = \rho_a U_5 \tilde{u},$$

where $\tilde{u}$ is the wave-induced wind-speed fluctuation. Root-mean-square values of

$\tilde{u}$ are probably of order $(ka)\,U_5 \sim 0{\cdot}1U_5$; if the r.m.s. attack angle variations are ± 5 degrees (they were estimated during the field experiments to be typically less than this), the dynamic pressure contamination from figure 3(*b*) is 5% of p_d at 5 m/sec. This gives

$$0{\cdot}05p_d \simeq 30 \times 0{\cdot}05 = 1{\cdot}5\,\text{dyne cm}^{-2}.$$

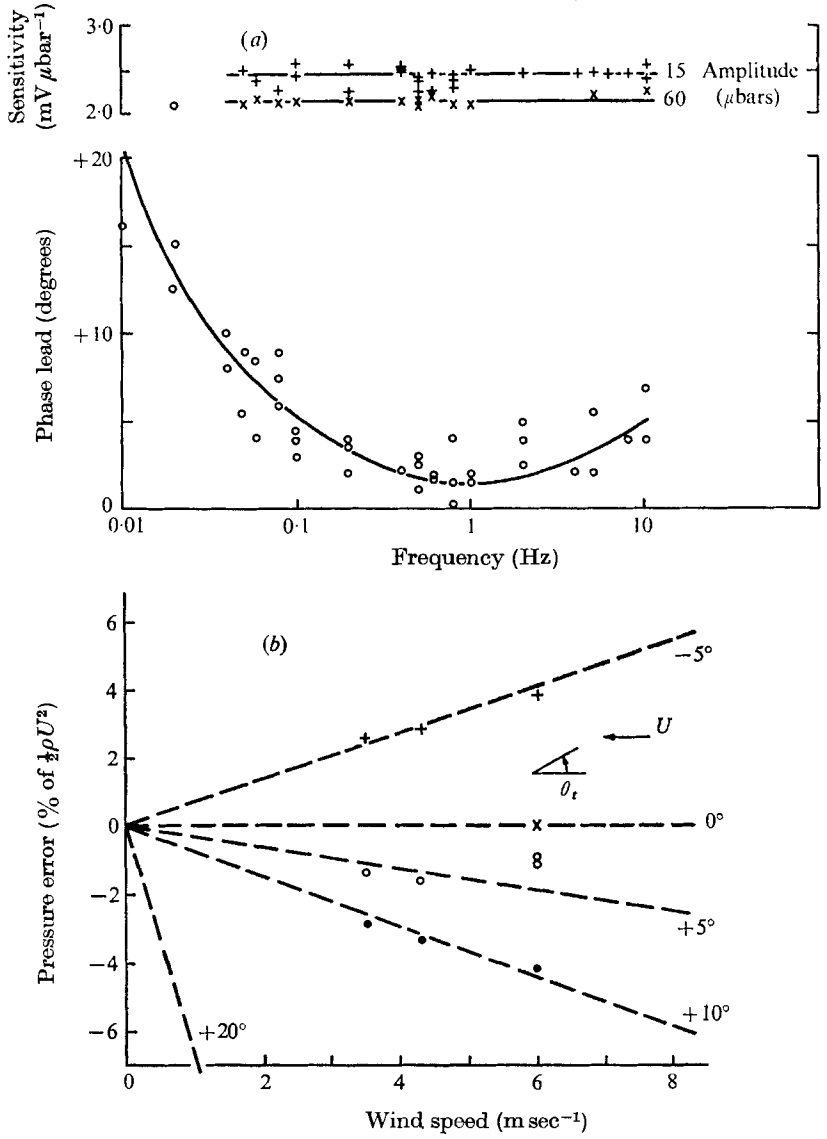

FIGURE 3. (*a*) Laboratory calibration of pressure measurement system. (*b*) Wind-tunnel calibration of buoy; pressure at sensing port versus wind speed for various tilt angles θ_t.

This is a 'worst case' calculation, but it serves to point out the large effects which dynamic pressure contamination may have. It probably introduced large spurious variations into the pressure signals of both Longuet-Higgins *et al.* (1963) and Kolesnikov & Efimov (1962).

4. Treatment and interpretation of the data

The ultimate goal was to obtain power and cross-spectra of the pressure and wave signals. Spectral analysis of the wave signal was straightforward. The pressure signal, on the other hand, required considerable preparation; the intermittent passage of water over the pressure-sensing diaphragm caused the recorded pressure signal to be interspersed with large spikes. In addition, the requirement for good low-frequency phase response led to serious drift problems. These and other contaminations were dealt with as described below.

4.1. *Analysis procedures*

The major part of the analysis was digital. All signals were digitized at an equivalent rate of 50 samples per second. Before sampling, matched low-pass constant time delay filters with a 3 db point at 6 Hz were applied to all signals. To minimize the effects of drift, the pressure signal was also passed through a simple RC high-pass filter with a cut-off frequency of 0·01 Hz. One run (run 4) was digitized by hand from a chart recording.

Spikes in the pressure signals were removed digitally (except for run 4, where they were smoothed out by hand); they were detected by their fast rise times, and replaced with the local mean of the pressure signal.

The non-linearities inherent in the capacitance wave probe used were removed digitally, and this treatment reduced errors to the level of $\pm$ 1 mm of differences in water level. In those runs where spike contamination of the pressure signal occurred, it was found (Dobson 1969) that phase errors in the cross-spectra between pressure and wave signals were minimized by replacing both signals with their local means during the time intervals when pressure spikes occurred.

The digital processing was carried out at the Computing Centre of the University of British Columbia. Power and cross-spectra for the pressure and wave signals, and sonic anemometer signals when available, were computed using the discrete Fourier transform technique of Cooley & Tukey (1965). The data points for a run were subdivided into 'blocks' of 1024 points each, and spectra computed for each block; the block spectral estimates were then averaged to give the final spectra. Also computed were the standard deviations of the spectral estimates from the blocks, giving the opportunity of looking not only at the spectral estimates but also at statistics on their variability over the run.

The power spectrum $\phi_{pp}(f)$ of the variable $p(t)$, for instance, is defined so that the integral under the spectrum over positive frequencies equals the variance of the signal

$$\int_0^\infty \phi_{pp}(f)\,df = \{v(p)\}. \tag{4.1}$$

The cross-spectrum between the variables $p(t)$ and $\eta(t)$ is

$$X_{p\eta}(f) = Co_{p\eta}(f) + iQu_{p\eta}(f); \tag{4.2}$$

it can also be put in terms of coherence and phase

$$Coh_{p\eta}(f) = \left[\frac{Co^2 + Qu^2}{\phi_{pp}(f)\,\phi_{\eta\eta}(f)}\right]^{\frac{1}{2}} \tag{4.3a,b}$$

and $$\theta_{p\eta}(f) = \tan^{-1}(Qu/Co).$$

A 'hanning' window was applied to all computed spectra.

The energy flux caused by the working of pressure forces on the waves is

$$\dot{E}(t) = -p(t)\,\partial\eta(t)/\partial t; \tag{4.4}$$

therefore an energy flux spectrum can be obtained from

$$\dot{E}(f) = \omega Q u_{p\eta}(f), \tag{4.5}$$

where $\omega = 2\pi f$, and the mean energy flux $\overline{\dot{E}}$ from the wind to the waves is

$$\overline{\dot{E}} = \int_0^\infty \dot{E}(f)\,df. \tag{4.6}$$

The spectrum of wave-supported momentum flux can then be written (Stewart 1961)

$$\tau_w(f) = \dot{E}(f)/c, \tag{4.7}$$

where $c = g/\omega$ is the phase speed of the waves. Therefore the mean wave-supported momentum flux is

$$\overline{\tau_w} = \int_0^\infty \frac{\omega \dot{E}(f)}{g}\,df$$

$$= \int_0^\infty \frac{\omega^2}{g} Q u_{p\eta}(f)\,df. \tag{4.8}$$

Since $\overline{\tau_w}$ is in fact a vector quantity a correction must be applied to allow for the fact that the wave field has a directional distribution. In this case a $\cos^2\theta$ distribution was assumed, where θ is the angle between wind and wave travel directions. Since waves extract momentum from the wind at a rate which varies as $\cos\theta$, the correction factor K to be applied is given by

$$K = \frac{2}{\pi}\int_{-\frac{1}{2}\pi}^{\frac{1}{2}\pi} \cos^3\theta\,d\theta \simeq 0{\cdot}85; \tag{4.9}$$

that is, all the measured $\overline{\tau_w}$ have been reduced by 15 %. Miles (1957) predicts $\zeta(f)$, the fractional rate of increase in wave energy per radian, for his inviscid laminar model; from (2.8) and (4.5)

$$\zeta(f) = \frac{Q u_{p\eta}(f)}{\rho_w g \phi_{\eta\eta}(f)}, \tag{4.10}$$

where E is given by $\frac{1}{2}\rho_w g\overline{a^2}$ and a is the wave amplitude. The spectral quantities of equations (4.5), (4.7) and (4.10) were computed for all the runs analyzed, and will be presented in § 5.

Standard errors of the mean over the number N of blocks analyzed are shown on all spectra as error bars for selected spectral estimates s_i; the standard error of the mean is given by

$$\text{S.E.} = \Big(\sum_N (s_i - \bar{S})^2/N(N-1)\Big)^{\frac{1}{2}}. \tag{4.11}$$

4.2. *Spikes in p(t)*

As has been mentioned, during most of the runs analyzed the pressure signal was interspersed with numerous 'spikes'. These spikes were caused by the washing of water over the top surface of the buoy; they were generally of large amplitude and were recognizable by rise times very short compared with the pressure signal itself. They lasted, in the sense that they obscured the signal, for periods of $\frac{1}{10}$ to 1 sec. They were removed during the digital analysis and replaced with the mean of the signal over the block in which they occurred. The presence of water on the buoy and hence the incidence of spikes was undoubtedly correlated with the wave height (that is, a spike was more likely to occur on the upwind slope than on the downwind slope of the wave).

In order to minimize phase errors due to such 'coherent spikes' it was necessary during the analysis to set the wave signal to zero during the spikes in the pressure signal, and to form the cross-spectrum between the 'spike-contaminated' signals $p_s(t)$ and $\eta_s(t)$ rather than between $p_s(t)$ and $\eta(t)$. To check that this procedure did minimize phase errors, cross-spectra were formed from computer-generated 'spike-contaminated' signals (Dobson 1969); phase errors were reduced to less than one degree by using the cross-spectrum between two 'spike-contaminated' signals. Coherences were, of course, enhanced by this procedure.

The spikes were found to cause distortions of the power and cross-spectra at frequencies greater than 1·5 Hz. At frequencies less than this the effect of spikes on the data was tested by comparing energy flux spectra obtained from data treated as described above with spectra obtained from blocks of shorter length scattered throughout the run, in which no spikes were detected. The results of this comparison for the four runs in which spikes occurred frequently is shown in figure 4. Such a comparison is not ideal in the sense that if discrepancies are found between 'spike-contaminated' and 'scattered clear block' spectra, they are not necessarily attributable to the spikes themselves; however, agreement between spectra computed in the two ways can be taken to indicate that the effect of the spikes on the data was small.

Of the four runs shown in figure 4 the agreement is good in two cases, fair in one (run 1), and poor in one (run 3). For this reason the spectra and integrals under them for run 3 are considered as suspect.

4.3. *Acceleration sensitivity*

The microphone diaphragm was mounted vertically and was therefore immune to vertical accelerations of the buoy on the waves; the rubber waterproofing diaphragm was not. The effect of response of the diaphragm to wave-induced accelerations would be to increase the magnitude of the co-spectrum between pressure and wave height; that is, to shift the apparent phase towards 180 degrees by an amount which increased as the square of the wave frequency.

The acceleration sensitivity of the whole buoy-mounted pressure sensing system was measured and found to be about 5 μbar/g; this would cause an increase of the magnitude of the observed co-spectra by 50 % at 1·5 Hz. Although this seems large, it will be seen that at frequencies above 1 Hz the co-spectra are

much smaller than the quadrature spectra, so the observed effect of such a sensitivity on the phase is small throughout the frequency range studied.

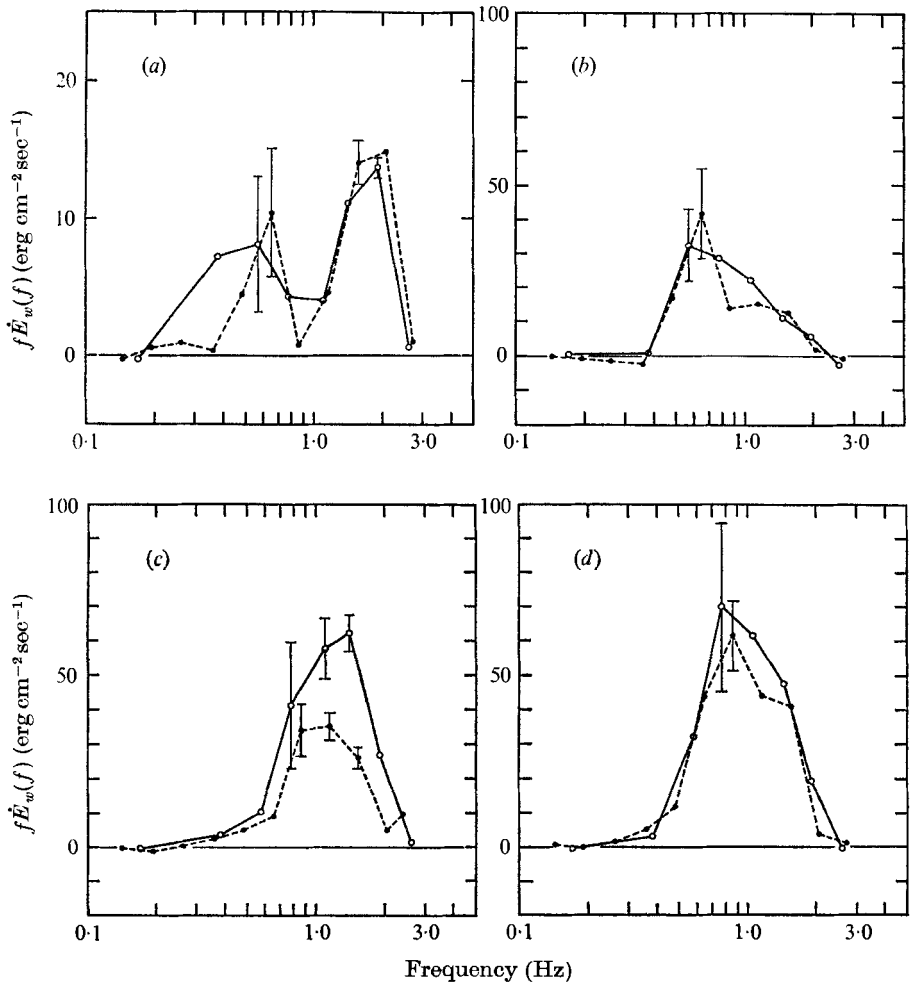

FIGURE 4. Comparison of $\dot{E}_w(f)$ computed from spike-contaminated (– – –) data and from clear, but randomly scattered (——) blocks of data, for runs: (*a*) 1; (*b*) 2*b*; (*c*) 3; (*d*) 6.

4.4. *The forced response of the buoy*

The buoy (see figure 2) was hinged, and its principal mode of forced response to the water surface was a tilting about the hinge which was resonant at about 2 Hz. From figure 3(*b*) it can be seen that changes of the angle of attack, that is of buoy tilt, cause concomitant dynamic pressure variations at the sensing port of the buoy. After extensive studies of slow-motion movies taken at various stages during the development of a buoy with suitable 'sea-keeping' characteristics, and noting that in all runs the wave spectra show maxima at 0·5 Hz, well below the resonant frequency of the buoy, it was concluded that the principal effect of the buoy pitching was to introduce a first harmonic into the pressure signal which

was in quadrature with the first harmonic of the waves. The Stokes first harmonic and the resulting coherent pressure contamination for a typical wave field (run 2*a* was used) was computed and from this the expected effect on $Qu_{p\eta}(f)$ at twice the wave frequency was found to be a 5–10 % reduction of the observed $Qu_{p\eta}(f)$ at this frequency.

The other possible effect of buoy pitching would be to cause small (but still perhaps important) tilt fluctuations at the wave frequency and in such a way that the spurious pressures thus produced were in quadrature with the waves. From figure 3 (*b*) at 5 m sec^{-1} a mean tilt error of two degrees (that is, $\pm$ 2 degrees) would cause a spurious pressure fluctuation with an amplitude of less than 1 % of $\frac{1}{2}\rho U^2$, or about 1·5 μbar. Such a signal, if it were exactly in quadrature with the waves, would produce a contribution to $Qu_{p\eta}(0{\cdot}5)$ of

$$Qu'_{p\eta}(0{\cdot}5) \simeq (1{\cdot}5)^2/2 \times 0{\cdot}1 = 11\,\mu\text{bar}^2\,\text{Hz}^{-1};$$

the measured *Co* and *Qu* at 0·5 Hz for run 2*a* were -60 and $-22\,\mu\text{bar}^2\,\text{Hz}^{-1}$, indicating an error of up to 50 % in $Qu(0{\cdot}5)$! This initially alarming result appears on closer scrutiny to be highly unlikely. The dynamic pressure fluctuations associated with buoy tilt are in antiphase with the tilt, a rise of the bow above its equilibrium position resulting in a decrease in pressure at the orifice. At frequencies below 2 Hz the failure of the buoy to respond to the waves would result in tilt errors which lagged the surface elevation, resulting in a spurious pressure signal which led the surface elevation. This amounts to a spurious damping signal, which would lessen the observed phase shifts of the pressure signal from 180 degrees. Since the observed phase shifts are already close to 90 degrees it is unlikely that the effect of buoy tilt can be significant.

4.5. *The finite size of the buoy*

The wavelength of the high-frequency waves becomes comparable with the size of the buoy at frequencies above 1 Hz. As a result the scales of variations in the wind speed which are associated with the wave motion become comparable with the buoy size, and so the wind speed at the bow of the buoy may differ significantly from that at the pressure port. This would cause spurious variations in pressure at the pressure port caused by a lack of complete rejection of the dynamic pressures existing over the port.

The lack of dynamic pressure rejection would result in a spurious *increase* in $Qu_{p\eta}(f)$ at high frequencies; the increase was found to be negligible ($< 0{\cdot}1$ %) at 0·6 Hz but could be as much as 30 % at 2 Hz (Dobson 1969). Thus the computed $Qu_{p\eta}(f)$ and therefore the $\dot{E}_w(f)$, $\tau_w(f)$ and $\zeta(f)$ spectra may be too high by as much as 30 % at frequencies above 2 Hz. Note that this effect tends to cancel the effect of the forced response of the buoy noted in § 4.4.

4.6. *Backscattering*

There was some reflexion of waves from the instrument mast, which was a 10 cm diameter cylinder located about 1 m to leeward of the buoy. Since the backscattered waves move against the wind they will presumably be damped by pressure fluctuations and their superimposition on the incoming waves will lead

to strongly wavelength-dependent errors in $Qu_{p\eta}(f)$. Since the coherence between incident and reflected waves falls off rapidly with frequency, and since the amplitude of the reflexions increases as the wavelength approaches the mast diameter, the backscattering effect can be expected to be largest at some intermediate frequency.

The effect of backscattering was computed from inviscid theory (Havelock 1940) and was found (Dobson 1969) to introduce increases of as much as 15 % in the wave power spectra near 1 Hz, but to be unimportant at frequencies above 2 Hz. $Qu_{p\eta}(f)$ was predicted qualitatively to be enhanced at 0·5 and 1·0 Hz and decreased at 0·8 and 1·2 Hz. Such effects are not visible in any of the computed power or cross-spectra.

5. Results and discussion

This work is based on the analysis of six runs, each lasting from 6 to 16 min, which were taken on waves at the Spanish Banks site during October and November 1967. A summary of relevant information is given in table 1. The runs are arranged in order of increasing wind speed. The wind speeds given were obtained from two cup anemometers at heights of about 3 and 5 m above mean water level; these were extrapolated to 5 m height using an assumed logarithmic profile and a drag coefficient of 0·0012 (Weiler & Burling 1967). The estimated accuracy of these speeds is ± 5 %. The over-water fetch was 40 km for run 1 and 1·5–6 km for the other runs. The mean currents in the water were obtained by timing pieces of tissue paper over known distances. Atmospheric stability was estimated from the difference between air temperature at a height of 3 m and water temperature at a depth of 10 cm, as measured with a thermistor having an estimated accuracy of $\pm 0{\cdot}1$ °C. Cases where the air–water temperature difference was within the stated uncertainty of the thermistor are called 'neutral' in the table.

5.1. *The power spectra*

The pressure and wave power spectra for run 2*a* are displayed in figure 5; this run was chosen because comparatively few spikes occurred in the pressure record. Logarithmic scales are used on both axes. Three spectra are shown: they are the wave and pressure power spectra and a spectrum of pressure to which has been added the quantity $\rho_a g\eta$, the out-of-phase pressure caused by the vertical motions of the buoy in the mean atmospheric pressure gradient.

The wave spectrum shows two peaks; these occurred in most of the runs. The low-frequency peak (0·2 Hz) is almost certainly caused by ship wakes; the higher-frequency peak (0·5 Hz) is associated with locally generated waves. At frequencies above the locally generated peak all the wave spectra have slopes between $-4{\cdot}5$ and -5.

The pressure spectra show appreciable excess energy in the regions of peaks in the wave spectra. The effect of adding $\rho_a g\eta$ varies with frequency; the low-frequency peaks in the pressure spectra are typically found to be eliminated by the addition of $\rho_a g\eta$ while the peaks at higher frequencies, although reduced in magnitude, are never eliminated.

Run no.	Time/date 1967 (Pacific std.)	Length of run (min)	Fetch (km)	Water depth (m)	5 m wind speed (cm sec^{-1})	Phase speed of dominant waves (cm sec^{-1})	Water current (cm sec^{-1})	State of tide	Atmospheric stability	Comments
5	1545/xi/17	12·0	1·0	3·0	150 (SE)	330	—	Slack	Stable	—
1	1940/x/16	16·3	40·0	2·4	220 (SW)	370	5	Slack	Unstable	Just after sunset
2*b*	2030/x/19	15·5	2·4	2·0	310 (ESE)	275	18	Falling	Unstable	Dark
2*a*	2010/x/19	11·0	2·4	2·1	320 (ESE)	270	18	Falling	Unstable	Dark
3	1435/x/20	16·8	6·7	2·8	340 (E)	225	5	Rising	Neutral	Air temp. rising
6	1225/xi/23	10·5	1·6	3·4	570 (ESE)	270	8	Slack	Neutral	Fine rain falling
4*b*	1200/x/30	3·1	2·4	2·7	700 (ESE)	305	30	Falling	—	—
4*a*	1150/x/30	4·0	2·4	2·7	800 (ESE)	265	30	Falling	—	—

TABLE 1. Information summary

5.2. *Cross-spectra*

The cross-spectra between the pressure (p) and wave (η) signals are displayed in terms of coherence and phase in figures 6 and 7. Figure 6 shows the p, η cross-spectra for all the runs, along with the p and η power spectra on linear scales; figure 7 shows the $p + \rho_a g\eta, \eta$ cross-spectra for selected runs. The suffix 's' denotes a signal from which spikes have been removed during the analysis process. Note that the cross-spectra are formed from the 'spike-contaminated' signals $p_s(t)$ and $\eta_s(t)$; see § 4.2. Phase corrections have been made in all cases to allow for the down-wind separation of the pressure and wave sensors (3·5 cm) and for the phase response of the pressure sensor. Note the different pressure scales in runs 4 (figures 6 (*e*), (*f*); 7 (*c*)) and 6 (figure 6 (*h*)). The gaps in the spectra, for instance at 1·3 Hz in run 1, are regions where appreciable noise contamination occurred. Two horizontal reference lines are provided at phases of 180 and −90 degrees.

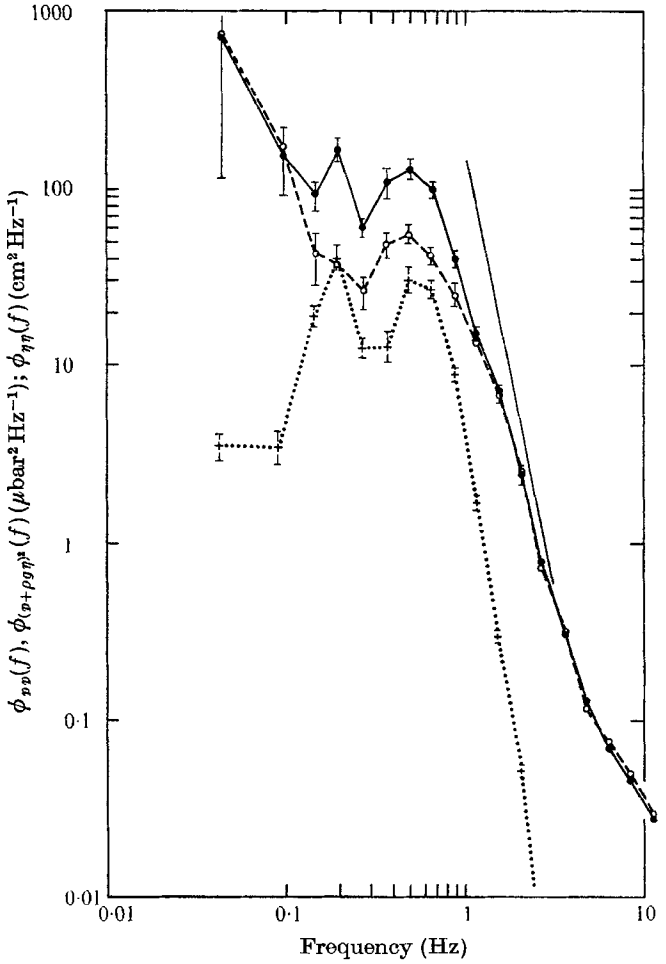

FIGURE 5. Log–log power spectra for a typical run 2*a*. —●—, pressure $p(t)$; – –○– –, $p(t) + \rho_a g\eta(t)$; · · · + · · ·, waves $\eta(t)$. The straight line has a slope of −5.

As mentioned in § 4, all information at frequencies greater than 1·5 Hz must be treated with a suspicion which rapidly mounts with increasing frequency. For the run lengths discussed, 0·3 is the lowest coherence at which the plotted phase can be assumed to convey useful information.

The prediction of potential flow theory for the fluctuating pressure p' at the surface of the water on which sinusoidal waves travel and over which blows a wind of speed U_0, uniform with height z, is

$$p' = -\rho_a g\eta\{1 + (1 - U_0/c)^2\} \tag{5·1}$$

(cf. Lamb 1932, § 232). This predicts wave-induced pressures in antiphase with the wave elevation, which can become many times $\rho_a g\eta$ if the wind opposes the waves. This prediction was used along with observed reductions in low-frequency coherence caused by the addition of $\rho_a g\eta$ to the pressure signals to estimate the sense of the swell direction in all the runs (Dobson 1969). Wind and swell were found to have come from the same direction in run 1 but were opposed in runs 3 and 5. Results for run 2*a* were ambiguous.

A striking feature of the figures is the high observed p, η coherences. Although these coherences are reduced to insignificant levels at swell frequencies by the addition of $\rho_a g\eta$, they are reduced little at the frequencies of the locally generated seas.

On each frequency scale in figures 6 and 7 a vertical arrow is to be found; this is the frequency f_k at which the wave phase speed equals the wind velocity at a height $k^{-1} = \lambda/2\pi$ above the water surface. It is used as an estimate of the frequency at which the cross-over occurs from wave damping to wave growth. The f_k values shown were determined using the deep-water wave dispersion relation and extrapolations from an assumed logarithmic wind profile. The height $\lambda/2\pi$ is used since it usually lies close to the height of one of the available cup anemometers.

The phase spectra show a similar pattern in all runs. At frequencies less than f_k they are mainly positive, indicating damping. Usually the transition to growth occurs at frequencies less than f_k. After the transition occurs the phase changes rapidly; indeed, the shift is almost discontinuous in the $p + \rho_a g\eta, \eta$ spectra. In some runs the phase shift from 180 degrees is as great as 75 degrees in the p, η spectra and often reaches 90 degrees in the $p + \rho_a g\eta, \eta$ spectra; maximum shifts from 180 degrees occur at frequencies higher than f_p, the frequency of the peak of the wave spectrum.

It might be argued that it would be more desirable for purposes of interpretation to present only the $p + \rho_a g\eta, \eta$ cross-spectra (a pressure sensor fixed in the air at a constant height above mean water level would measure something more related to $p + \rho_a g\eta$ than to the 'quasi-Lagrangian' buoy p signal). The $p + \rho_a g\eta, \eta$ cross-spectra are not emphasized, for the simple reason that sizable additional errors are introduced into the phase spectra by the addition of $\rho_a g\eta$ (Dobson 1969); furthermore, it is a relatively simple matter to convert theoretically predicted phase angles to the co-ordinate system of the buoy.

Figure 8 displays a plot of phase shift θ' of the pressure from 180 degrees (90 degrees means p lags η by this amount) against the dimensionless parameter

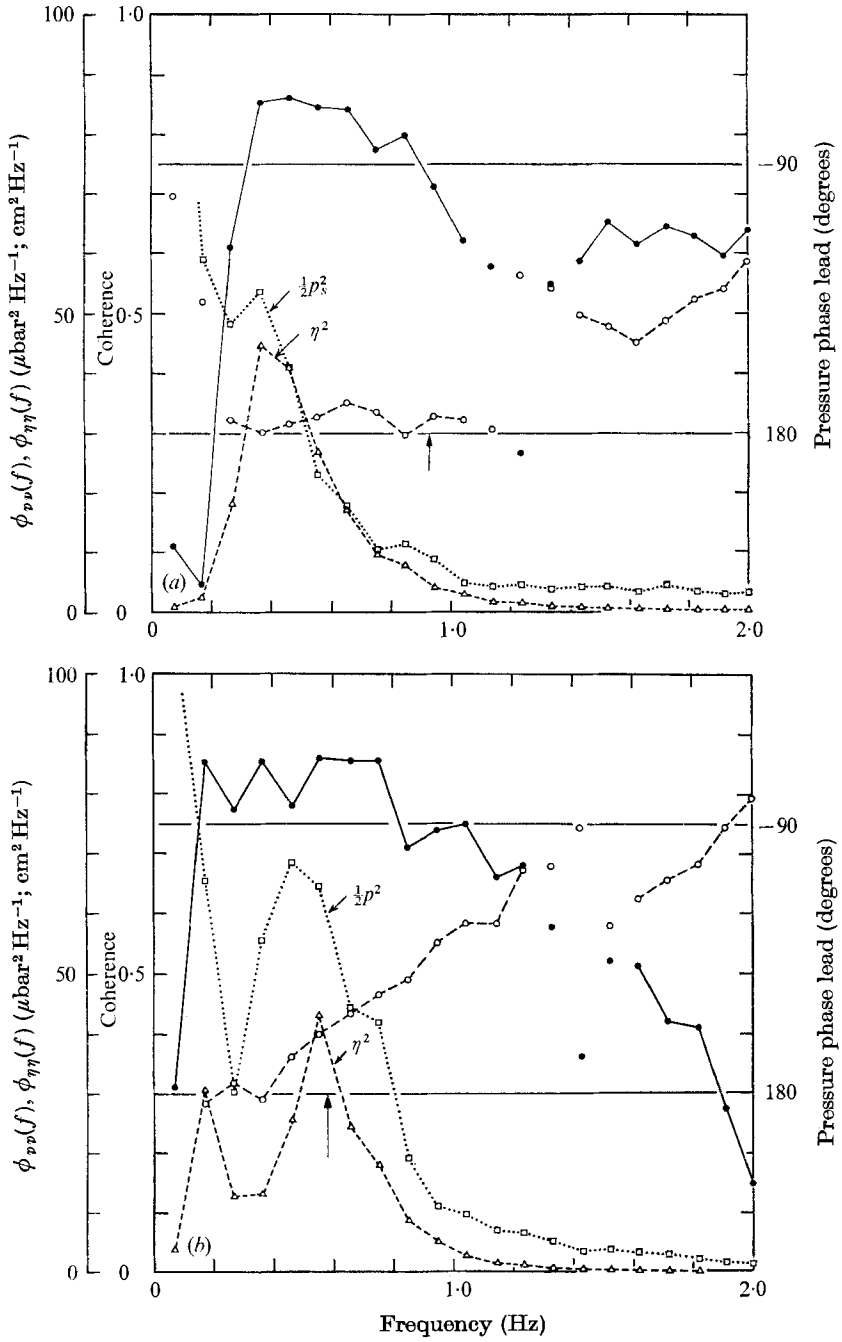

FIGURE 6. For legend see p. 112.

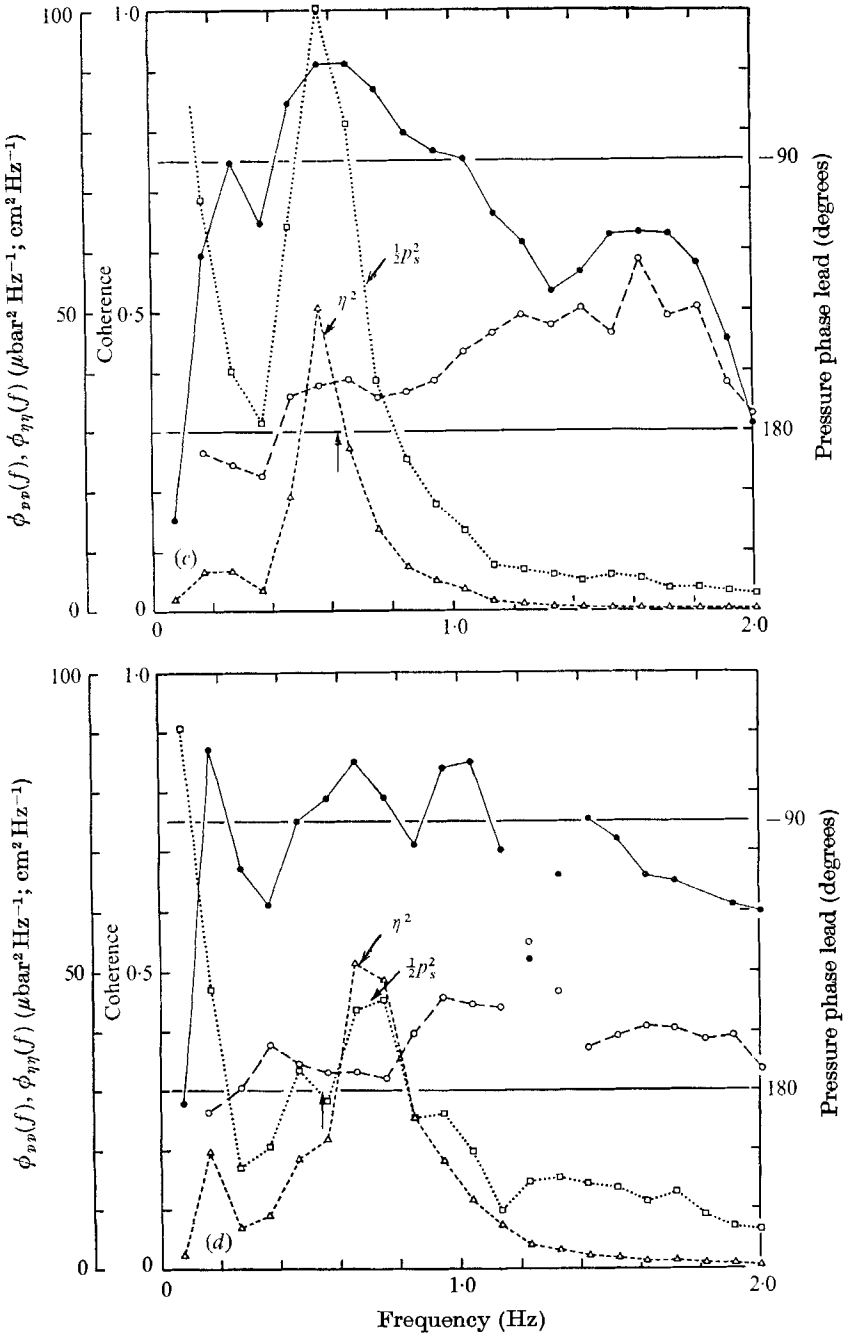

FIGURE 6. For legend see p. 112.

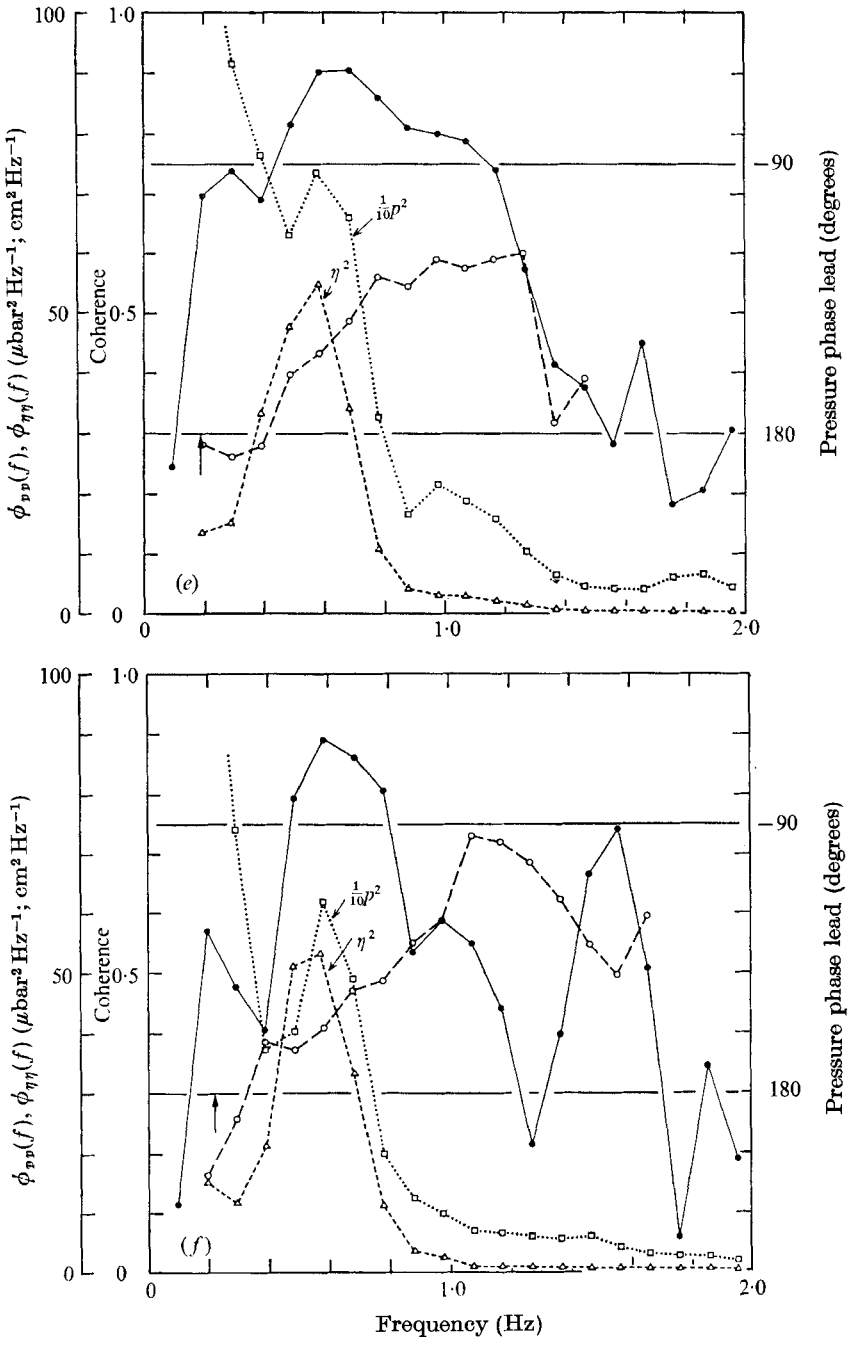

FIGURE 6. For legend see p. 112.

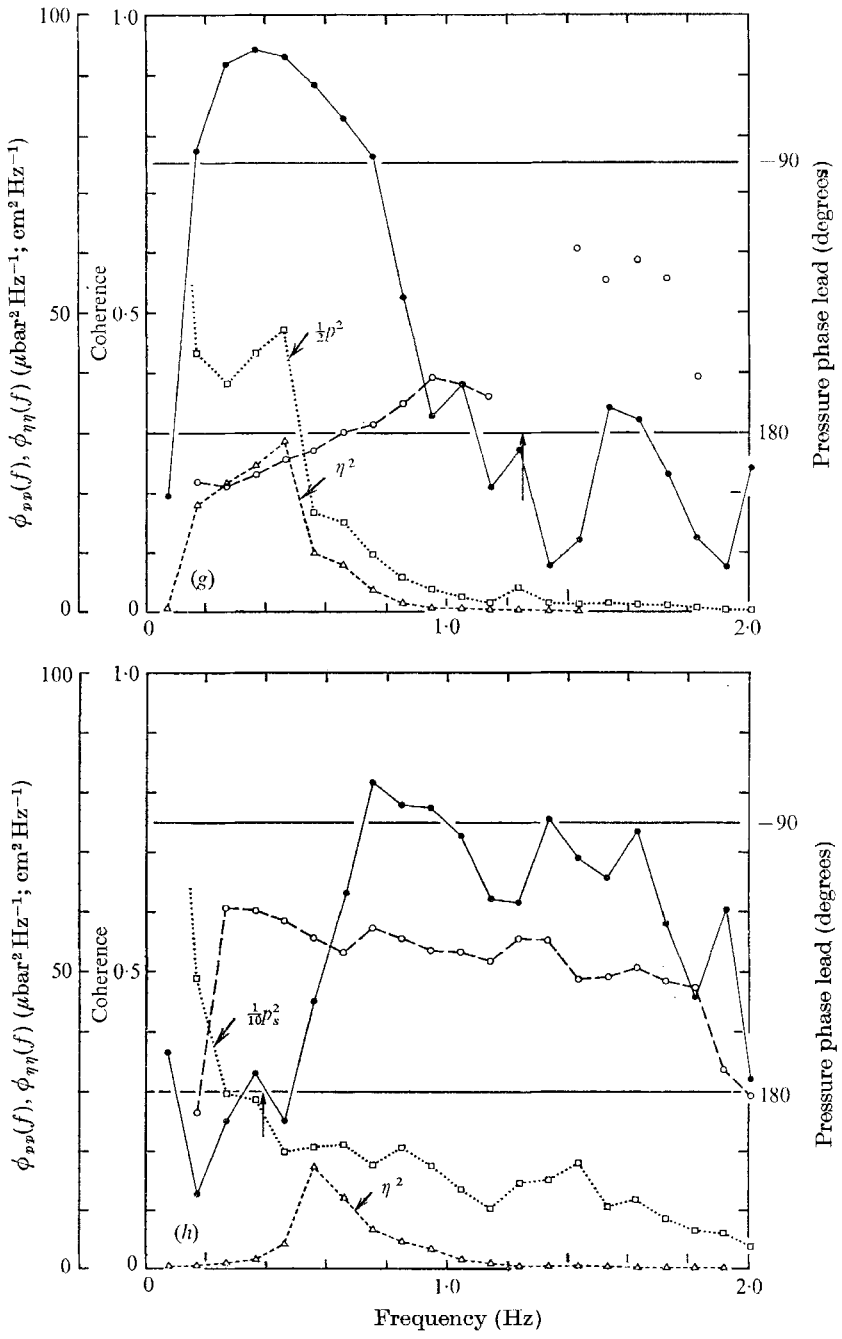

FIGURE 6. Cross-spectra of $p(t)$ and $\eta(t)$ expressed as coherence (—●—) and phase (– –○– –); linear power spectra of $p(t)$ (· · ·□· · ·) and $\eta(t)$ (– –△– –) for all runs. (*a*) Run 1; (*b*) 2*a*; (*c*) 2*b*; (*d*) 3; (*e*) 4*a*; (*f*) 4*b*; (*g*) 5; (*h*) 6.

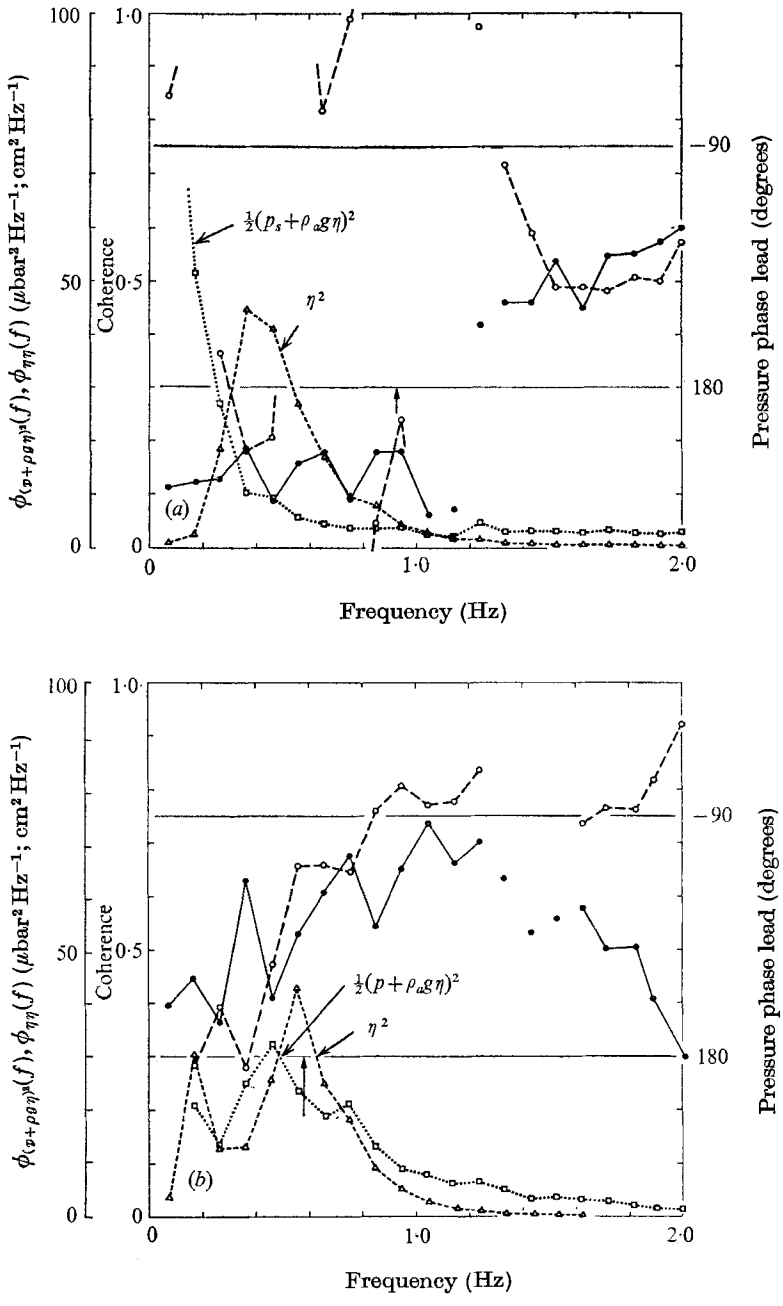

FIGURE 7. For legend see p. 114.

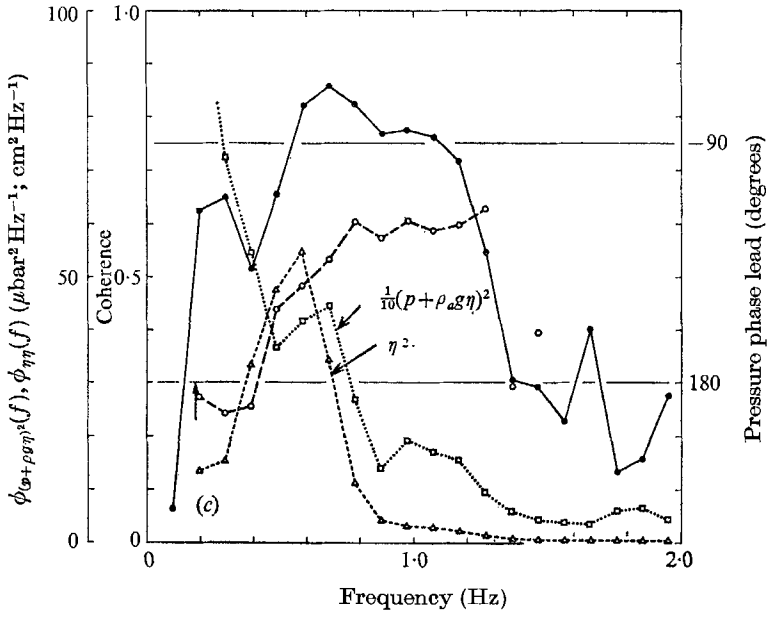

FIGURE 7. Cross-spectra of $p(t)+\rho_a g\eta(t)$ and $\eta(t)$ expressed as coherence (—●—) and phase (– –○– –); linear power spectra of $p(t)+\rho_a g\eta(t)$ (· · ·□· · ·) and $\eta(t)$ (– –△– –), for runs: (*a*) 1; (*b*) 2*a*; (*c*) 4*a*.

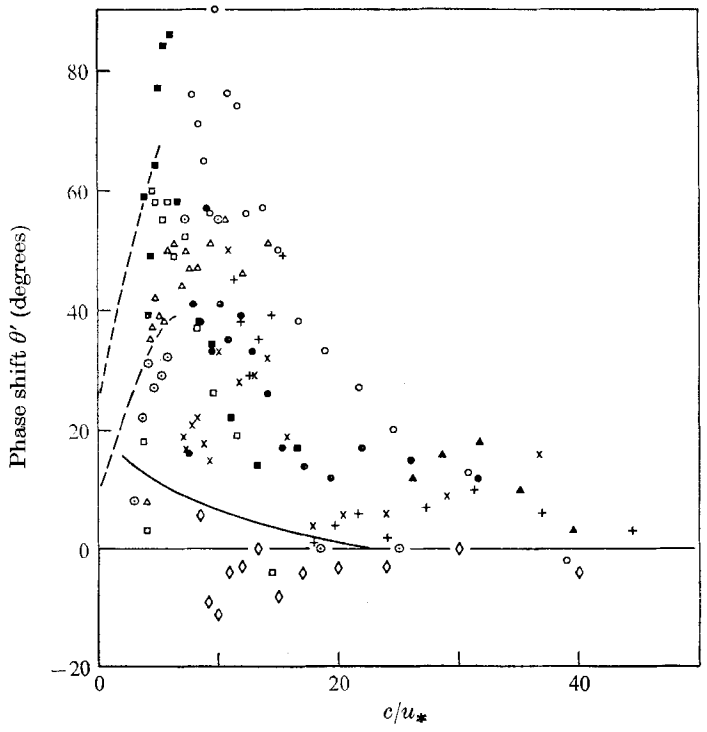

FIGURE 8. Phase shift of pressure signal from 180 degrees plotted against c/u_*. +, run 1; ○, run 2*a*; ●, run 2*b*; ×, run 3; □, run 4*a*; ■, run 4*b*; ▲, run 5; △, run 6; ◇, Longuet-Higgins *et al.* (1963); ⊙, Shemdin & Hsu (1967); – – –, envelope of Kendall's (1970) wind-tunnel results; ——, Miles's (1959) theoretical prediction.

c/u_*; here u_* is taken to be $U_5/29$, the value obtained by assuming a drag coefficient of 0·0012. Included with the experimental phase shifts are the predictions of Miles's (1959) inviscid laminar model as modified by Longuet-Higgins *et al.* (1963) to account for buoy motion (equation (2.13) in this paper), and results from Longuet-Higgins *et al.*, Kendall (1970, pressures over waves in rubber in a wind tunnel), and Shemdin & Hsu (1967, wind-water tunnel). The graph shows first that Miles's predictions fall far short of the phase shifts observed in this experiment for $5 < c/u_* < 20$. Furthermore, although the scatter is large, the field and the wind-tunnel results agree reasonably well except for the results of Longuet-Higgins *et al.* (1963), which only agree with the present results at high c/u_* (where the authors say their phase errors are smallest—roughly $\pm$ 10 degrees). Note that the agreement is considerably improved if the phases from run 3 are ignored. Considering the results of the analysis of spike contamination (see figure 4 and the text in § 4.2), it may well be that the phase angles from this run are considerably in error.

Although the buoy data agree fairly well with Kendall's phases at $c/u_* = 5$, they appear to fall towards zero at $c/u_* \leqslant 4$, whereas Kendall's results show a 20-degree phase shift at $c/u_* \simeq 0$. Differences in the two measurements at low c/u_* may be real; Kendall worked at low (and zero) wave speeds and moderate wind speeds to obtain phases at low c/u_*, whereas the present low c/u_* results apply to high wind speeds and moderate wave speeds. This is, to reduce c/u_* Kendall reduced c, keeping a Reynolds number based on wavelength roughly constant, while reduced c/u_* in this experiment was obtained by looking at higher u_*, which means an increase in Reynolds number. This Reynolds number dependence may mean that even at low c/u_* the turbulence can be an important factor in the wave growth process.

5.3. *Energy and momentum flux spectra*

Spectra of the energy and momentum fluxes from the wind to the waves were determined from the p, η quadrature spectra as follows:

$$\dot{E}_w(f) = 2\pi f Q u_{p\eta}(f)\,\delta f, \tag{5.2}$$

$$\tau_w(f) = \frac{\dot{E}(f)}{c} = \frac{4\pi^2 f^2}{g} Q u_{p\eta}(f)\,\delta f, \tag{5.3}$$

where δf is the bandwidth of the spectral estimates. The spectra for representative runs are shown along with the relevant wave spectra in figure 9. Note the different vertical scales used for run 4.

Run 5 was taken during a glassy calm; the only wave energy present was due to wakes from passing ships, and these waves travelled against what wind there was (it rose toward the end of the run to 250 cm sec^{-1}). A three-dimensional sonic anemometer was in operation during the run and large wave-induced vertical and horizontal velocities were recorded. Figure 9 (*g*) clearly shows that considerable damping occurred at the wave frequencies, and both the buoy and the sonic anemometer registered a *negative* (upwards) momentum transfer. The run was taken as a 'noise' test to see what effect buoy motion and electronics system

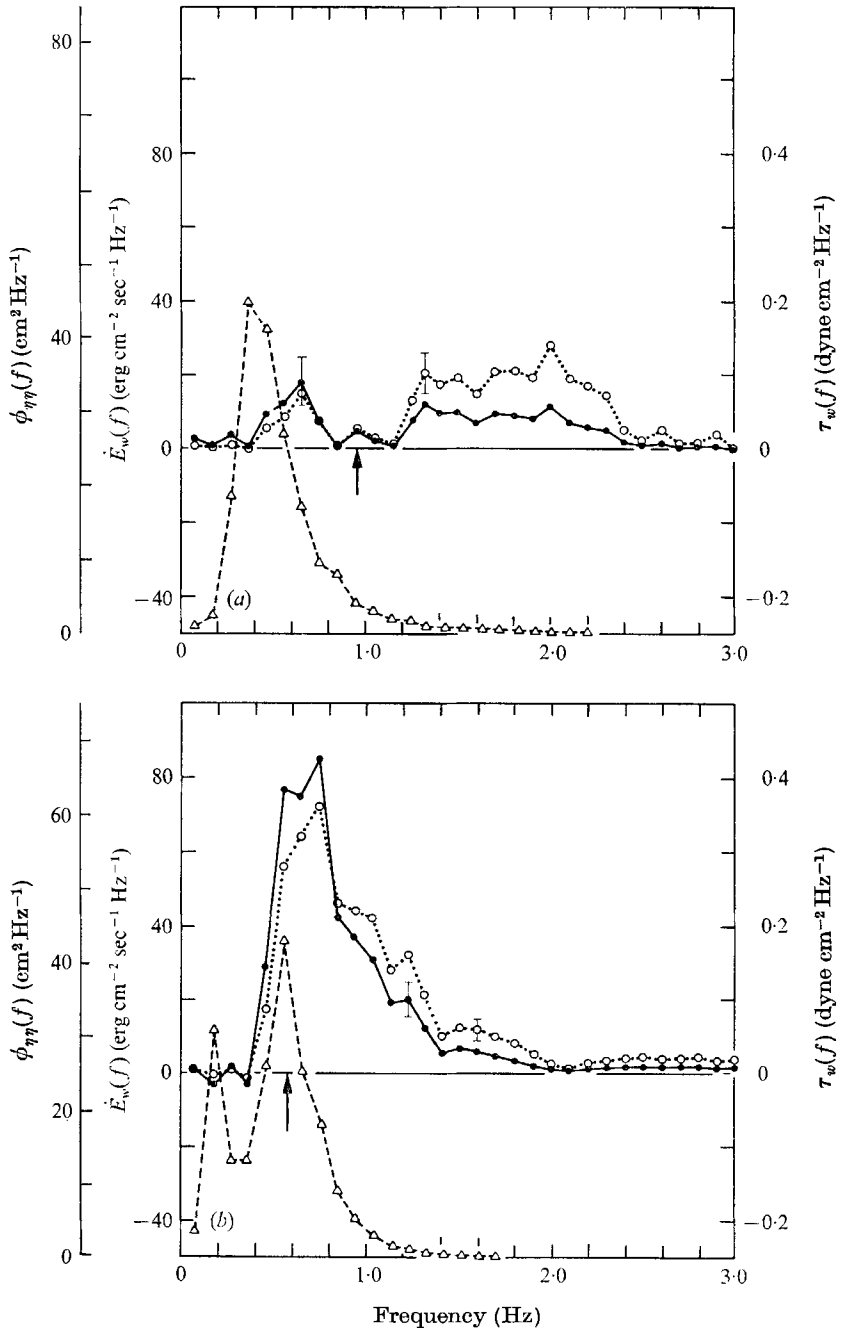

FIGURE 9. For legend see p. 119.

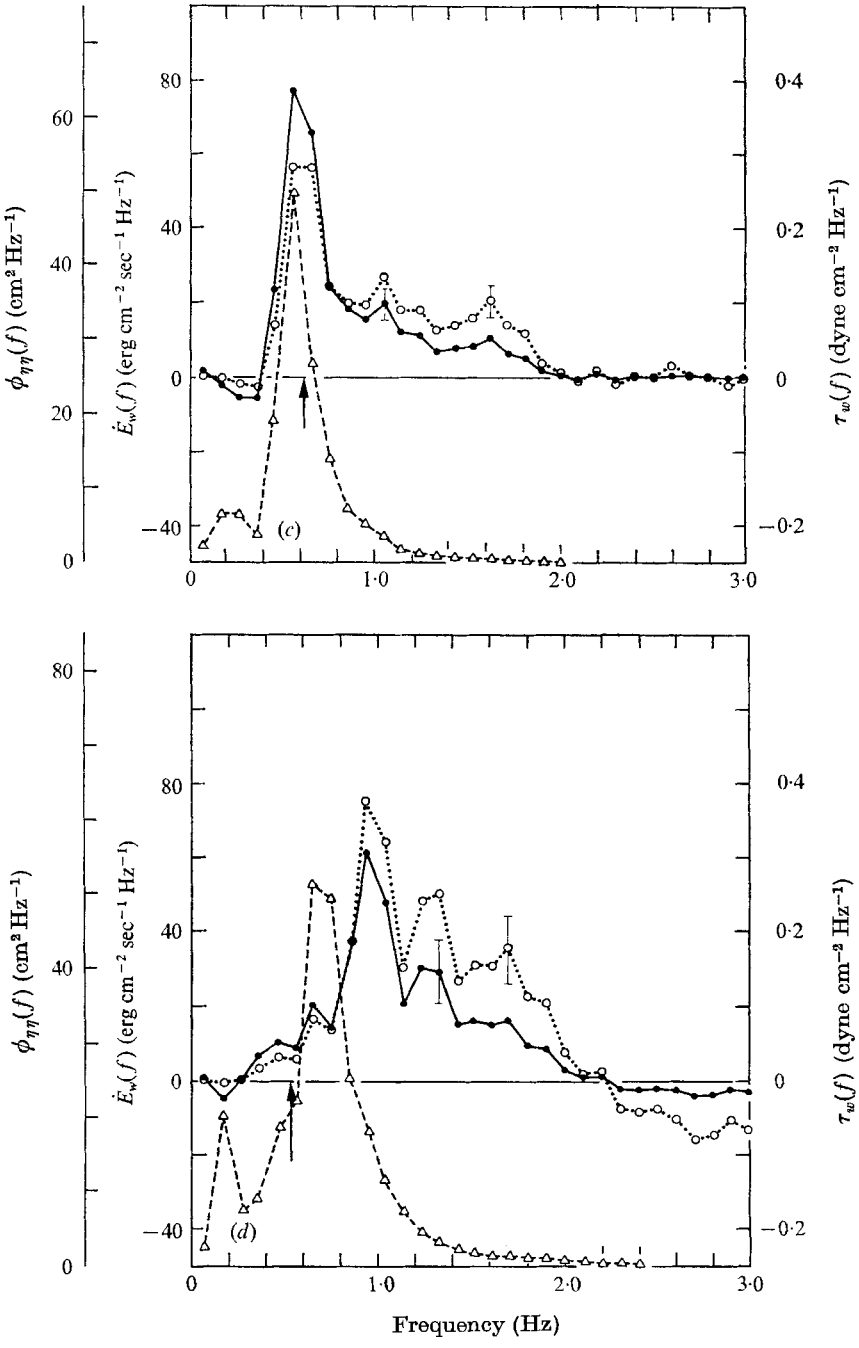

FIGURE 9. For legend see p. 119.

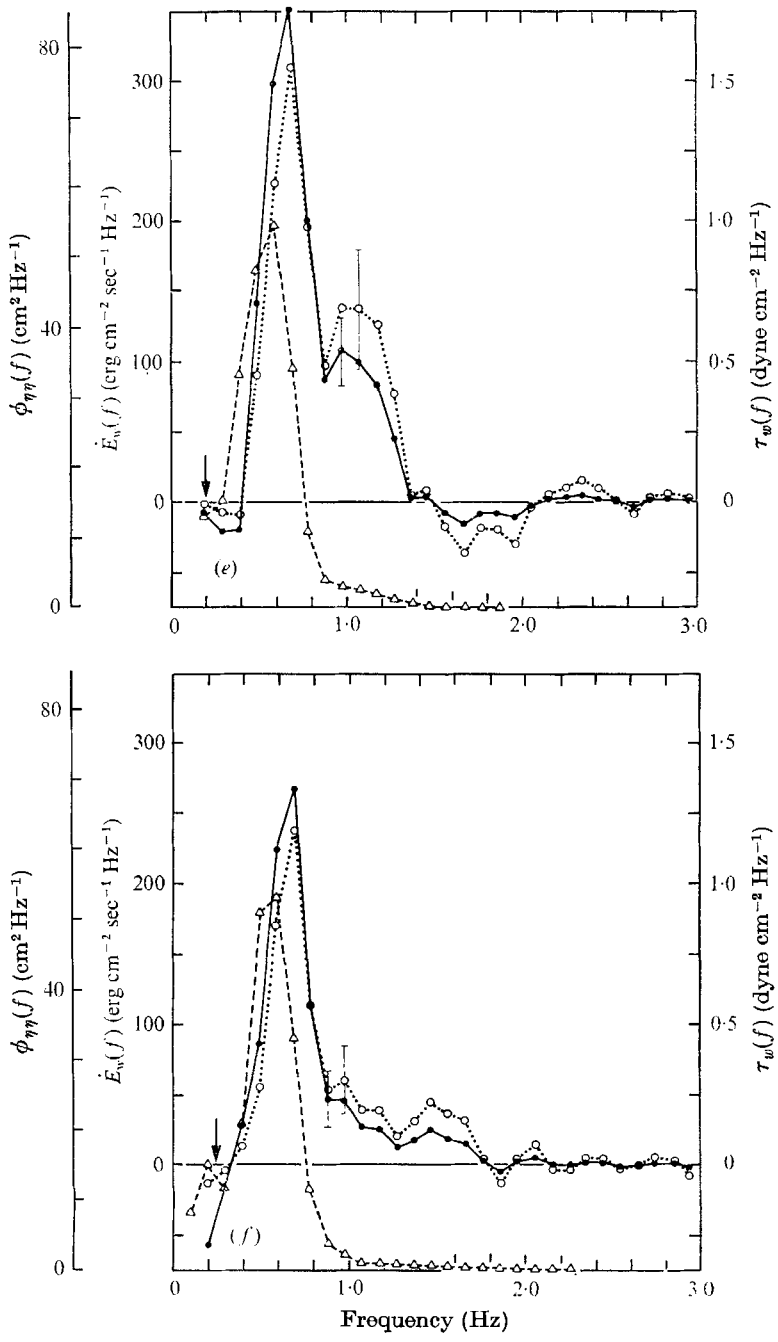

FIGURE 9. For legend see p. 119.

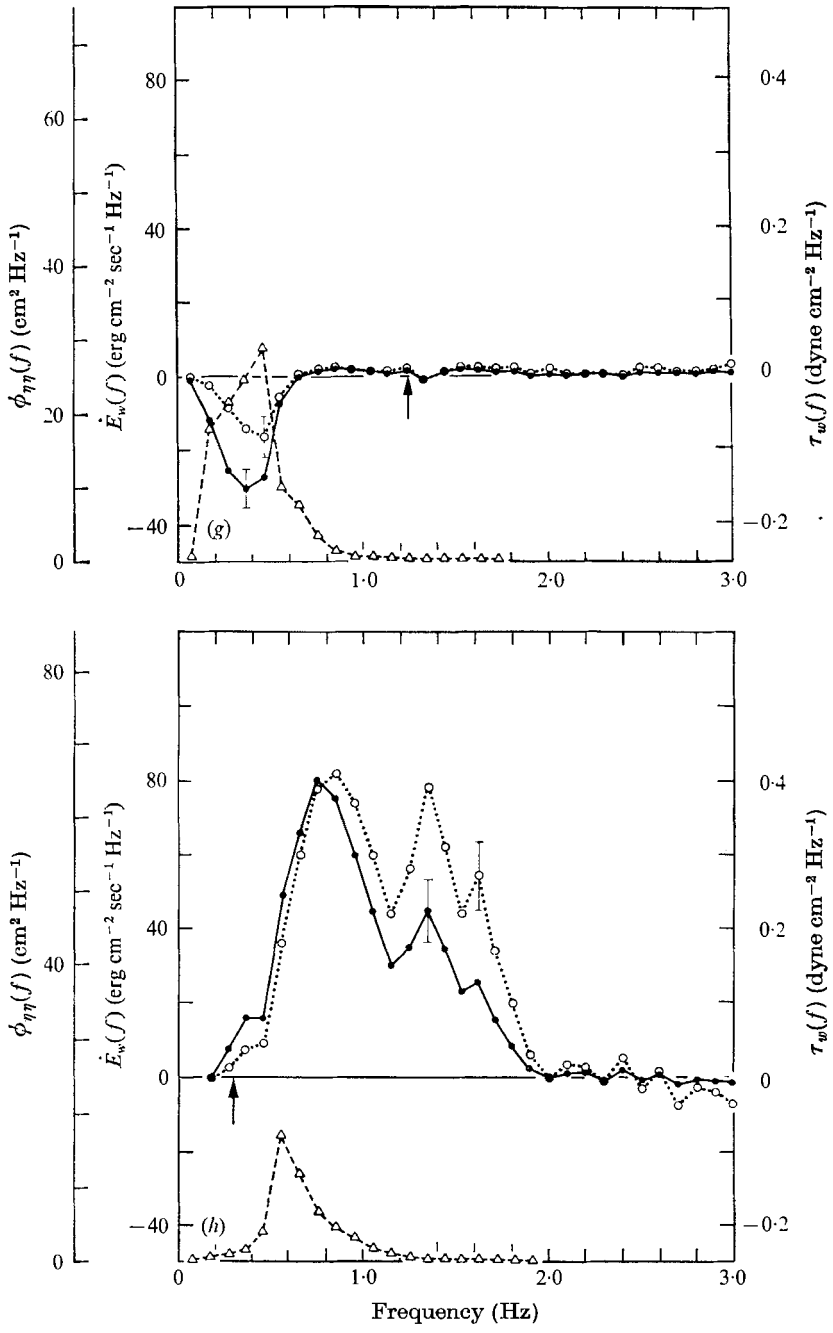

FIGURE 9. Wave-supported energy and momentum flux spectra, linear wave spectra for runs: (*a*) 1; (*b*) 2*a*; (*c*) 2*b*; (*d*) 3; (*e*) 4*a*; (*f*) 4*b*; (*g*) 5; (*h*) 6. —●—, $\dot{E}_w(f)$; --○--, $\tau_w(f)$; --△--, $\phi_{\eta\eta}(f)$.

noise had on spectral regions where no waves were present and only very small pressure fluctuations occurred. The negligible observed $\dot{E}_w$ and τ_w values at frequencies above 0·6 Hz indicate low noise in these spectral regions. It should be mentioned that this was *not* a test for the acceleration sensitivity of the buoy sensor; that is dealt with in § 4.

The 2–3 Hz frequency range is included in the graphs principally to show the behaviour of the $\dot{E}_w$ and τ_w spectra in regions where all spectral components are expected to be spurious, being caused by noise of one kind or another (see § 4). The small negative energy and momentum fluxes at low frequencies are presumably real, being associated with wave damping.

One of the interesting facts about the flux spectra is that they generally attain their maximum values at frequencies higher than that of the peaks in the wave spectra. This is to be expected since at a given wind speed a high-frequency wave receives energy faster than a low-frequency wave of the same energy.†

It is also possible that energy is being transferred down the spectrum by processes not detected in this experiment, such as, for instance, the 'sideband feeding' mechanism suggested by Benjamin & Feir (1967). Transfer by wave-induced variations in surface tangential stress (Stewart 1967; Longuet-Higgins 1969) might also be possible, although it is more likely to be important for high-frequency waves with large slopes.

The second interesting fact concerning the τ_w spectra in particular is their extremely narrow bandwidth (typically 0·4–2·0 Hz). In comparison, a typical $-\rho_a \overline{uw}$ spectrum measured within a few metres of the mean water level is broad, containing significant energy at frequencies from 0·01–10 Hz (figure 10). It will be shown in the following section that the wave-supported stresses obtained by integrating under the τ_w spectra account for a large percentage of the total wind stress. This means that in the first few metres (or perhaps centimetres) above the water surface all the momentum being transferred by the large and small scales of the turbulent motion must be 'funnelled' into the wave-induced shearing motion. This implies a strong interaction between the turbulent and wave-induced Reynolds stresses near the water surface, and indicates, as suggested by Phillips (1966) and Miles (1967), that the wave generation process is greatly influenced by the interplay between turbulent and wavy shear flows near the water surface.

5.4. *Mean energy and momentum fluxes*

Integrals (see (4.6), (4.8)) to obtain $\dot{E}_w$ and τ_w (table 2) were truncated at 2·0 Hz to avoid contributions due to noise (for run 1 the integration was extended to 3·0 Hz). In the table c_p is the phase speed of the dominant waves, $\bar{\tau}_s$ is $-\rho_a \overline{uw}$ as measured with a sonic anemometer, τ_c is computed from

$$\bar{\tau}_c = 0{\cdot}0012 \rho_a U_5^2 \tag{5.4}$$

and

$$C_{Dw} = \bar{\tau}_w / \rho_a U_5^2. \tag{5.5}$$

Energy fluxes to the waves have been computed only once before, by Kolesnikov & Efimov (1962); although there are good reasons (see § 1) for

† I am indebted to a referee for this suggestion.

doubting the validity of those workers' data, their values of $\dot{E}_w$ fall close to the values given in the table.

Run	U_5 (cm sec^{-1})	c_p/u_*	$\dot{E}_w$ (erg cm^{-2} sec^{-1})	$\sigma_{\dot{E}}$ (erg cm^{-2} sec^{-1})	$\bar{\tau}_w$ (dyne cm^{-2})	σ_τ (dyne cm^{-2})	$\bar{\tau}_s$ (dyne cm^{-2})	τ_w/τ_c	$C_{Dw} \times 10^3$
5	150	—	−5	7	−0·04	0·02	−0·002	—	—
1	220	49	13	17	0·11	0·11	—	1·6	1·8
2*b*	310	26	29	18	0·16	0·11	—	1·1	1·3
2*a*	320	25	43	18	0·24	0·10	—	1·6	1·9
3	340	19	30	32	0·19	0·26	—	1·1	1·3
6	570	14	60	32	0·38	0·22	0·49	0·8	0·95
4*b*	700	13	230	230	0·45	0·30	—	0·6	0·75
4*a*	800	10	155	185	0·66	0·36	—	0·7	0·83
							Average	1·1	1·3

TABLE 2. Integrated mean fluxes of energy and momentum to the waves

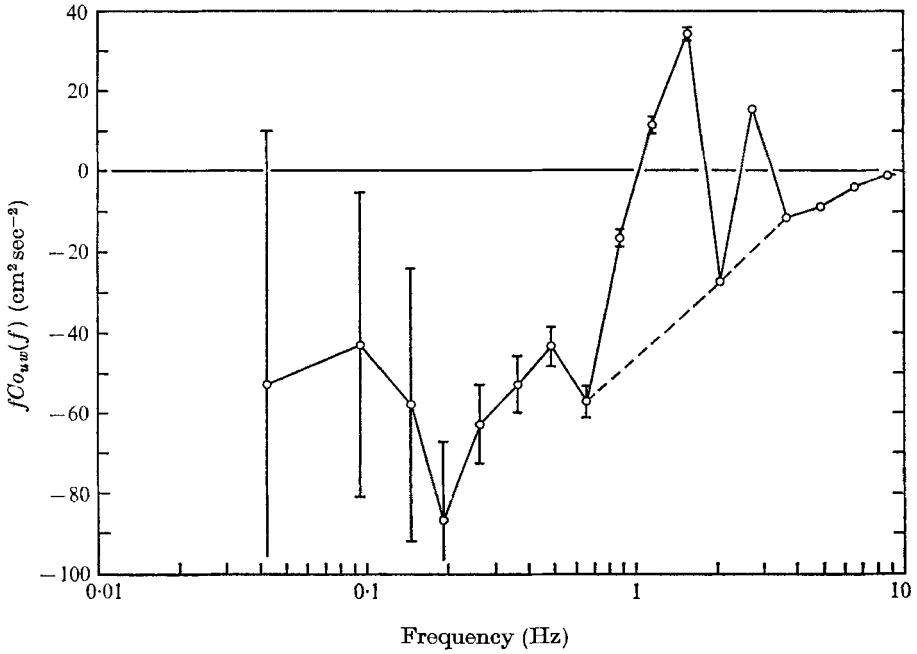

FIGURE 10. Total momentum flux ($-\rho_a \overline{uw}$) spectrum for run 6. Dotted lines show estimated spectrum in noisy region.

Speculation concerning the fraction $\bar{\tau}_w/\bar{\tau}$ of wave-supported to total wind stress has been going on for some time (Stewart 1961). The measurements of the fraction given in the table provide strong indications, but no firm conclusion, as to the size of $\bar{\tau}_w/\bar{\tau}$. There is no significant difference between the average $\bar{\tau}_w$ and the average $\bar{\tau}_c$ in the runs analyzed; in fact, all the C_{Dw} values fall within the combined standard deviations of the C_D values determined by Smith (1967) and

Weiler & Burling (1967), who measured total wind stress using two different methods at the same site as the present one!

Of the two cases for which stresses measured by a sonic anemometer are available for comparison with momentum fluxes from the buoy, run 5 is of no direct interest here since no active wave generation occurred. Unfortunately, in run 6 neither $\bar{\tau}_w$ nor $\bar{\tau}_s$ was well measured. The estimated accuracy of the pressure sensor calibration is $\pm 20\,\%$. The sonic $\overline{uw}$ co-spectrum for run 6 is shown in figure 10. It has obviously been modified by noise; also 35 % of the total $\overline{uw}$ covariance occurred below 0.04 Hz. To obtain $\overline{uw}$ the integration under the spectrum was performed under the dotted curve in the figure, which is a smoothed estimate of the true form of the spectrum in the 0·7–4 Hz region ($\bar{\tau}_s$ computed from the original, noise-contaminated spectrum is 30 % lower than that presented in the table). If $\pm 20\,\%$ errors are assigned to $\bar{\tau}_s$ and $\bar{\tau}_w$ then

$$\bar{\tau}_w/\bar{\tau}_s = 0{\cdot}8 \pm 30\,\%. \tag{5.6}$$

Since the comparison of the $\bar{\tau}_w$ with the $\bar{\tau}_c$ is inconclusive, this single measurement represents the best estimate available from these data of the size of the fraction $\bar{\tau}_w/\bar{\tau}$.

It should be noted that run 6 is in some ways a special case. The range of c/u_* in the run was $4 < c/u_* < 14$, compared with the range over all the runs of $4 < c/u_* < 50$. Furthermore, the wave spectrum was small. This may have been due to the short fetch, and thence it may be that the wave field was varying rapidly with fetch; the light rain falling at the time may also have influenced the result.

The question of why the high-frequency $\dot{E}_w$ and τ_w spectra go to zero at relatively low frequencies is hard to answer from the available data. There is some evidence (Van Dorn 1953) that considerable momentum transfer is associated with the presence of high-frequency components in the wave field; on the other hand it appears that a large fraction of the total momentum transfer from wind to water is accounted for by the buoy measurements.

Thus it seems that the findings of this experiment are in conflict with those of Van Dorn. On the other hand, if it is assumed that the small, short waves act as some sort of catalyst to the 'low-frequency' growth mechanism observed in this experiment, then the fall-off of the high-frequency end of the momentum and energy flux spectra at relatively low frequencies and the large measured momentum transfers reported here can be explained without direct conflict with Van Dorn's finding that the elimination of high-frequency components from a wave field results in significant reduction in the total momentum flux to the water surface.

5.5. *The ζ spectra*

Spectra of ζ, the fractional rate of acquisition of wave energy per radian as defined by (2.8), are given for four of the runs in figure 11. Three curves are presented. ζ_M is the prediction scaled from Miles's (1959) paper; ζ_{SC} is derived from an empirical relation used by Snyder & Cox (1966) to fit their measurements of wave growth:

$$\zeta_{SC} = \frac{\rho_a}{\rho_w}\left(\frac{U_\lambda}{c} - 1\right), \tag{5.7}$$

where U_λ is the wind speed at a height one wavelength above the mean sea surface; the third curve has been faired through the 'observed' points from this experiment.

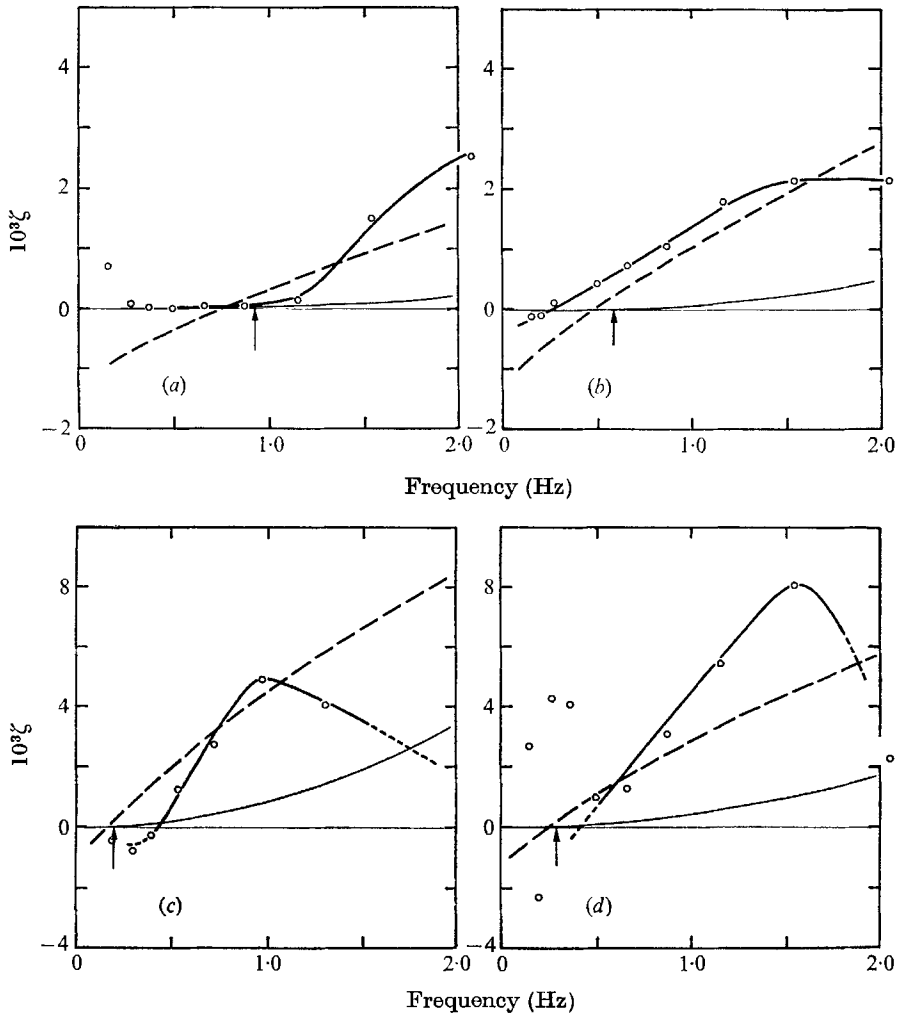

FIGURE 11. Spectra of ζ for runs: (*a*) 1; (*b*) 2*a*; (*c*) 4*a*; (*d*) 6. —○—, this experiment; — —, Snyder & Cox (1966); ——, Miles's (1959) theoretical prediction ζ_M.

The observed values lie roughly along the Snyder & Cox lines, confirming their finding that the Miles inviscid laminar model underpredicts observed wave growth rates by factors of five to eight. Whereas the present measurements were of energy input, the Snyder & Cox measurements were of wave growth down a fetch. The fact that the two different measurements agree indicates either that in the Snyder & Cox experiment little wave energy was lost along the fetch because of wave breaking, etc., or that the energy lost was being replaced by some process not associated with growth by quadrature pressures. The major difference between the present observations and those of Snyder & Cox is a high-frequency

fall-off in ζ which they did not observe. Since the fall-off occurs at frequencies where the present data are rapidly becoming unreliable, strong conclusions are unwarranted; on the other hand, since the observed wave-supported momentum fluxes are essentially as large as the total wind stress, it would be suspicious if ζ did *not* fall off at high frequencies (a wave-supported momentum flux larger than the total wind stress would be difficult to explain). Snyder & Cox integrated equation (5.7) above to obtain an estimate of wave-supported wind stress, and the lack of high-frequency (that is, low c) fall-off in equation (5.7) probably accounts for the unreasonably large drag coefficient, 7×10^{-3}, that they calculated.

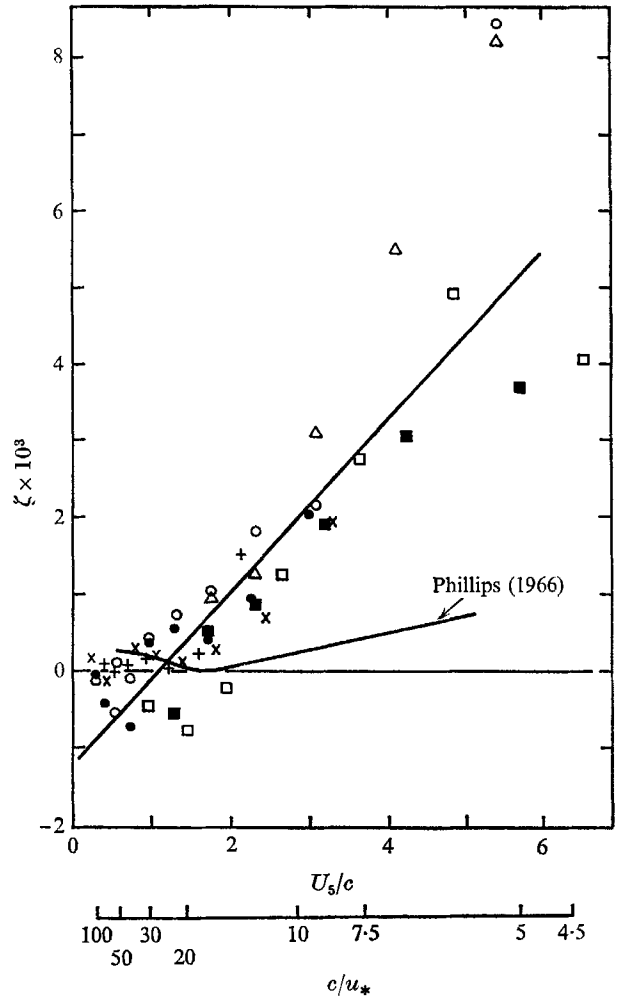

FIGURE 12. Dimensionless plot of ζ versus c/u_*. +, run 1; ○, run 2*a*; ●, run 2*b*; ×, run 3; □, run 4*a*; ■, run 4*b*; △, run 6; ——, Phillips's (1966) theoretical prediction.

A dimensionless grouping of measured values of ζ for all the runs in which wave generation occurred (figure 12) does not show any information taken at frequencies above 1·5 Hz. Reduction in the frequency range presented has the effect of

removing the high-frequency ζ fall-off noted in previous paragraphs; the fall-offs are not scaled by the parameter c/u_*. The c/u_* scale is obtained by multiplying c/U_5 by 29. The line through the points is arbitrarily forced to pass through $-\rho_a/\rho_w$ at U_5/c equals zero; its slope is estimated by eye (the many assumptions and possibilities for error which are inherent in the plotted points preclude the use of more quantitative fitting procedures). It is found to pass through ζ equals zero at $U_5/c \simeq 1$, and fits the equation

$$\zeta \simeq \frac{\rho_a}{\rho_w}(U_5/c - 1) \tag{5.8}$$

(the Snyder & Cox relation (5.7) also fits the points moderately well).

The theoretical ζ curve shown on the figure was obtained by Phillips (1966), who included the effects of the turbulent and wavy Reynolds stresses in his solution of the Orr–Sommerfeld equation. The effect of these additional terms is to cause the predicted ζ curve to rise with increasing c/u_* above $c/u_* \simeq 20$; this does not seem consistent with the observations.

Longuet-Higgins (1970; personal communication) has noted that the form of (5.8) leads to a relation for the quadrature pressure which resembles Jeffreys' original assumption (equation (2.1)). Thus if the rate of working $\dot{E}_w$ of the pressure forces is

$$\dot{E}_w = -\overline{p^* \partial\eta/\partial t}, \tag{5.9}$$

and if the energy E per unit area of the wave field is

$$\omega E = \rho_w \overline{c(\partial\eta/\partial t)^2}, \tag{5.10}$$

then from (2.8) and (5.8)

$$p^* = -s^* \rho_a (U - c)\, \partial\eta/\partial t. \tag{5.11}$$

Here s^* is an empirical sheltering coefficient, which is conveniently equal to 1·0! Note also that the factor $(U-c)$ appears in (5.11), instead of $(U-c)^2/c$ as in (2.1).

6. Conclusions

The experiment obtained an accurate measurement of the phase relation between normal pressure and wave height at the surface of wind-driven sea waves over a range of c/u_* from 5 to 50. The measured phase shifts from 180 degrees far exceed those predicted by Miles's (1959) inviscid laminar model of wave generation. Although highly scattered, the phase shifts agree tolerably well with the laboratory measurements of Shemdin & Hsu (1967) and Kendall (1970).

The quantities $\dot{E}_w(f)$ and $\tau_w(f)$, respectively the energy and momentum fluxes from the wind to the waves, were determined from the p, η quadrature spectra. The energy and momentum flux spectra are all sharply peaked at frequencies at or above that of the peak of the locally generated waves.

Integrations under the $\tau_w(f)$ spectra were performed for all runs; the values for the wave-supported wind stress $\bar{\tau}_w$ so obtained were compared with empirical estimates and in one case with an actual measurement of the total wind stress $\bar{\tau}$; the comparisons indicate that for sea waves $\bar{\tau}_w/\bar{\tau}$ is close to one, and is most probably about 0·8.

The fractional increase in wave energy per radian $\zeta(f)$ was compared with the predictions of Miles's inviscid laminar model and with an empirical relation which fits the wave growth data of Snyder & Cox (1966); the agreement with the Snyder & Cox relation was good, while the inviscid laminar model was found to underpredict ζ by factors of five to eight.

A dimensionless plot of ζ versus c/u_*, where u_* is the friction velocity obtained assuming a constant drag coefficient, was fitted well with the simple relation (5.8) for the range $6 < c/u_* < 50$.

I am deeply indebted to my supervisors, R. W. Stewart and R. W. Burling, and to my fellow students J. F. Garrett, J. A. Elliott and J. R. Wilson; all contributed invaluable advice and assistance. The spectral analysis programs were written by Garrett and Wilson at the U.B.C. Computing Centre. The work was supported by the U.S. Office of Naval Research under contract NRO 083–207. I am also thankful for suggestions and advice from S. D. Smith and D. M. Garner of Bedford Institute, where this paper (Bedford Institute Contribution no. 230) was written.

REFERENCES

BENJAMIN, T. B. 1959 Shearing flow over a wavy boundary. *J. Fluid Mech.* **6**, 161.

BENJAMIN, T. B. & FEIR, J. E. 1967 The disintegration of wave trains on deep water. *J. Fluid Mech.* **27**, 417.

COOLEY, J. W. & TUKEY, J. W. 1965 An algorithm for the machine calculation of complex Fourier series. *Math. Comput.* **19**, 297.

DAVIS, R. E. 1969 On the high Reynolds number flow over a wavy boundary. *J. Fluid Mech.* **36**, 337.

DAVIS, R. E. 1970 On the turbulent flow over a wavy boundary. *J. Fluid Mech.* **42**, 721.

DOBSON, F. W. 1969 Observation of normal pressure on wind-generated sea waves. Ph.D. Dissertation, Institute of Oceanography, University of British Columbia.

HAVELOCK, T. H. 1940 The pressure of water waves upon a fixed obstacle. *Proc. Roy. Soc.* A**175**, 409.

JEFFREYS, H. 1925 On the formation of water waves by wind. *Proc. Roy. Soc.* A**110**, 341.

KENDALL, J. M. 1970 The turbulent boundary layer over a wall with progressive surface waves. *J. Fluid Mech.* **41**, 259.

KINSMAN, B. 1960 Surface waves at short fetches and low wind speeds—a field study. *Chesapeake Bay Inst., Johns Hopkins University Tech. Rep.* **19**, 175.

KOLESNIKOV, A. G. & EFIMOV, V. V. 1962 Apparatus for the measurement of the energy transmitted to ocean waves by the normal pressure of the wind. *Okeanologia, ANSSSR*, **4**, 505.

LAMB, H. 1932 *Hydrodynamics* (6th edition). Cambridge University Press.

LIGHTHILL, M. J. 1962 Physical interpretation of the mathematical theory of wave generation by wind. *J. Fluid Mech.* **14**, 385.

LONGUET-HIGGINS, M. S. 1969 Action of a variable stress at the surface of water waves. *Phys. Fluids*, **12**, 737.

LONGUET-HIGGINS, M. S. 1970 Recent ideas on the generation of waves by wind. Verbal Presentation at *IUGG-IAMAP-AMS Conference on Planetary Boundary Layers*, Boulder, Colorado; March 1970.

LONGUET-HIGGINS, M. S., CARTWRIGHT, D. E. & SMITH, N. D. 1963 Observations of the directional spectrum of sea waves using the motions of a floating buoy. *Ocean Wave Spectra*, pp. 111–32. Prentice-Hall.

LUMLEY, J. L. & PANOFSKY, H. A. 1964 *The Structure of Atmospheric Turbulence.* Interscience.

MILES, J. W. 1957 On the generation of surface waves by shear flows. *J. Fluid Mech.* **3**, 185.

MILES, J. W. 1959 On the generation of surface waves by shear flows. Part 2. *J. Fluid Mech.* **6**, 568.

MILES, J. W. 1960 On the generation of surface waves by turbulent shear flows. *J. Fluid Mech.* **7**, 469.

MILES, J. W. 1967 On the generation of surface waves by shear flows. Part 5. *J. Fluid Mech.* **30**, 163.

PHILLIPS, O. M. 1957 On the generation of waves by turbulent wind. *J. Fluid Mech.* **2**, 417.

PHILLIPS, O. M. 1966 *The Dynamics of the Upper Ocean.* Cambridge University Press.

PLATE, E. J., CHANG, P. C. & HIDY, G. M. 1969 Experiments on the generation of small water waves by wind. *J. Fluid Mech.* **35**, 625.

SHEMDIN, O. H. & HSU, E. Y. 1967 The dynamics of wind in the vicinity of progressive water waves. *J. Fluid Mech.* **30**, 403.

SMITH, S. D. 1967 Thrust anemometer measurements of wind-velocity spectra and of Reynolds stress over a tidal inlet. *J. Mar. Res.* **25**, 239.

SNYDER, R. L. & COX, C. S. 1966 A field study of the wind generation of ocean waves. *J. Mar. Res.* **24**, 141.

STEWART, R. H. 1970 Laboratory studies of the velocity field over deep-water waves. *J. Fluid Mech.* **42**, 733.

STEWART, R. W. 1961 The wave drag of wind over water. *J. Fluid Mech.* **10**, 189.

STEWART, R. W. 1967 Mechanics of the air-sea interface. *Phys. Fluids, Supplement: Boundary Layers and Turbulence,* **10**, S47.

VAN DORN, W. G. 1953 Wind stress on an artificial pond. *J. Mar. Res.* **12**, 249.

WEILER, H. S. & BURLING, R. W. 1967 Direct measurements of stress and spectra of turbulence in the boundary layer over the sea. *J. Atmos. Sci.* **24**, 653.

WU, JIN 1970 A criterion for determining air-flow separation from wind waves. *Tellus,* **21**, 707.

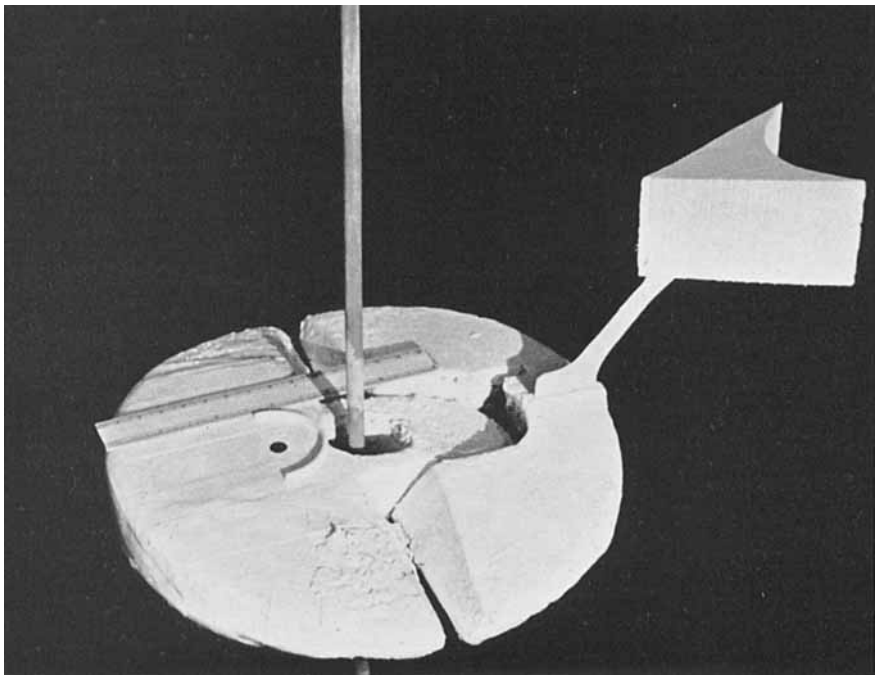

FIGURE 2. Buoy and wave probe, showing location of pressure-sensing port.